

Acceleration and Diffusion of
Cosmic Rays from Supernova Remnants
in a Multiphase Interstellar Medium

Soonyoung Roh

A thesis presented for the degree of
Doctor of Science

Laboratory for Theoretical Astronomy & Astrophysics (Ta-Lab)
Department of Physics, Nagoya University
Furo-cho, Chikusa-ku, Nagoya, Aichi 464-8602 Japan

Acceleration and Diffusion of Cosmic Rays from Supernova Remnants in a Multiphase Interstellar Medium

「多相星間媒質中の超新星残骸における
粒子加速と宇宙線粒子の伝搬」

Soonyoung Roh

A thesis presented for the degree of
Doctor of Science

Laboratory for Theoretical Astronomy & Astrophysics (Ta-Lab)
Department of Physics, Nagoya University
Furo-cho, Chikusa-ku, Nagoya, Aichi 464-8602 Japan

Abstract

Supernova remnants (SNRs) have long been believed to be the source of hadronic Galactic cosmic rays (GCRs) up to energies of the ‘knee’, near 5×10^{15} eV, of the cosmic ray (CR) spectrum. Supernova explosions forming collisionless shock waves induce the shocked gas and relativistic particles (hereafter cosmic rays) that produce multi-wavelength thermal and nonthermal emission. Diffusive shock acceleration (DSA) is the most promising mechanism for converting the kinetic energy of a supernova explosion into energetic particles (A.R. Bell, (1978a;1978b); R.D. Blandford & J.P. Ostriker (1978); W.I. Axford et al. (1977)) and plays an important role in non-thermal emission during the overall process, e.g., (W.I. Axford et al. (1977); W.I. Axford et al. (1982); L.O. Drury & H.J. Vlok (1981)). In the framework of DSA, an individual charged particle experiences nearly elastic collisions with background plasma and gains energy by shock crossing. This leads to a non-thermal CR spectrum of the power-law form $N(\varepsilon) \sim \varepsilon^{-2}$. Shock acceleration by DSA in SNR shocks is associated with transport effects in the Galaxy, and some of the highest energy CRs inevitably escape from their acceleration sites (by a so-called diffusion process) due to interactions with turbulent magnetic fields. Observations support highly efficient acceleration, and a significant fraction of the energy of SNRs may go into escaping CRs if DSA is efficient. However, it is unclear how the CRs escape from SNRs and propagate into interstellar space.

Several studies of escaping CRs have already been done and observed a strong spatial correlation between TeV emission and the

molecular gas distribution at the Galactic Center (F.A. Aharonian et al. (2006); E. Wommer et al. (2008); D. Ballantyne et al. (2007)). Recent observations succeeded in detecting pion-decay gamma rays from CR protons, and the pion signature in the gamma ray energy spectra of SNRs RX J1713.7-3946 and RX J0852.0-4622 (Y. Fukui et al. (2012)) is similarly located to the gamma ray emission and CO+HI emission. The pion-decay signature in SNRs is believed to be evidence for protons accelerated in SNRs (M. Ackermann et al. (2013)) interacting with molecular clouds (A.A. Abdo et al. (2009,2010a,2010b,2010c); M. Tavani et al. (2010); Y. Ohira et al (2012)).

The actual gamma ray emission from pion decay should depend on the diffusion of CRs in a multiphase interstellar medium with molecular clouds (T. Inoue et al. (2012)). In order to quantitatively analyse the diffusion of high-energy CRs from acceleration sites, we have performed test-particle numerical simulations of CR protons using three-dimensional magnetohydrodynamics (MHD) simulations of an interstellar medium swept up by a blast wave. We analyse the diffusion of CRs over a length scale of order a few parsecs in one-phase medium that are provided by the Richtmyer-Meshkov instability in our simulated post-shock region of SNRs, and investigate the possibility of a superdiffusive process in CR propagation and acceleration in SNRs. Although we find evidence of superdiffusion (travel distance $\propto t^{0.75}$) in our simulations, its effect on high-energy (30 TeV) CR diffusion over the length scale of the turbulence in SNR is limited. On the contrary, we find the diffusion of CRs is accurately described by a Bohm diffusion coefficient, which may support the interpretation of high-energy emission from SNRs, at least for particles with energies above 10 TeV, in a realistic interstellar medium.

Contents

1	Introduction	3
1.1	Energetic Particles in Astrophysics	3
1.2	Basic Properties of the Interstellar Medium	8
1.2.1	Overview of the Interstellar Medium (ISM)	8
1.2.2	Global ISM Models: Five Phases of the ISM	12
1.3	Cosmic-Ray Acceleration and Observations of Gamma Ray	15
2	Dynamics of the Interstellar Medium	19
2.1	Magnetohydrodynamics (MHD)	19
2.2	Approximations of Magnetohydrodynamics	20
2.2.1	Ideal MHD Equations	24
2.2.2	MHD Waves: Alfvenic and Magnetosonic Waves	26
3	Acceleration of Cosmic Rays	30
3.1	Cold Plasma	30
3.1.1	Introduction to Cold Plasma	30
3.1.2	Wave Equations	31
3.1.3	Cold Plasma Dielectric Permittivity	32
3.1.4	Wave Propagation Parallel to the B_0 : $\theta = 0^\circ$	36

3.1.5	Whistler Waves	40
3.2	Resonance of Particles	44
3.2.1	Resonance in Unmagnetized Plasma	44
3.2.2	Resonance in Magnetized Plasma	45
4	Numerical Simulations of the Diffusion of Cosmic Rays	48
4.1	Hydrodynamics Simulations	48
4.2	Description of Simulation Settings	58
4.2.1	Test Particle Simulations	58
4.2.2	Initial Settings	60
4.2.3	Runge-Kutta Method Error	64
4.3	Diffusion Process in a One-Phase Medium	67
4.3.1	Diffusion in Configuration Space	67
4.3.2	Comparison with Bohm Diffusion Rate	73
4.3.3	Superdiffusion	76
4.3.4	Richardson Diffusion	80
4.3.5	Diffusion in Energy Space	81
4.3.6	Effect of Electric Field	81
4.4	Diffusion Process in a Multiphase Medium	84
4.4.1	Diffusion in Configuration Space	84
4.4.2	Comparison with Bohm Diffusion Rate	86
4.5	Magnetic Field Lines	91
5	Summary and Future Work	97
	Acknowledgement	107

Chapter 1

Introduction

1.1 Energetic Particles in Astrophysics

1. What are Cosmic Rays?

Cosmic Rays (CRs) are high-energy charged particles; they travel into our Solar System from far away in the Galaxy. Referred to as Galactic Cosmic Rays (GCRs), their composition is well known. Most of the components of GCRs consist of protons ($> 90\%$) and electrons, and atomic nuclei ($< 1\%$) which pass through the Galaxy. The CR energy distribution has been observed up to 10^{20} eV from high-energy experimental observatories such as a HiRes (cite), Auger (cite), Telescope Array (cite), and so on. Such high-energy particles are difficult to observe directly at the ground, so it is difficult to determine their origin. Because CRs are charged particles, CRs do not travel in straight lines in space. Their trajectories are often bent by intergalactic or interstellar magnetic fields. As a result, it is difficult to investigate the original source of CRs from arrival direction only. Also, as we mentioned above, it is difficult to directly detect CRs at the Earth due to the rarity of UHECR events.

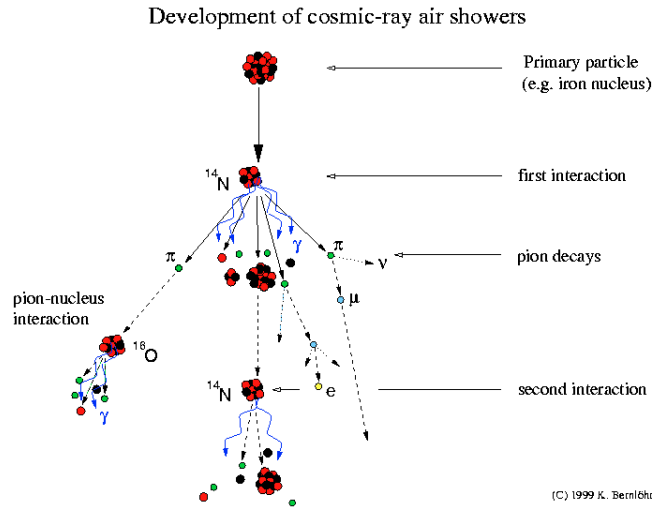


Figure 1.1: Cascade of cosmic ray air showers. When CRs enter the Earth’s atmosphere, they first collide with air molecules of oxygen or nitrogen; subsequently through complex interactions and cascades, extensive air showers (EASs), which are made of up to hundreds of billions of secondary particles, are generated (B. Rossi & K. Greisen (1941); J. Knapp et al. (2003)). By detecting the photons produced by secondary particles and/or the secondary particles arriving at the ground, the properties of primary particles such as the energy, arrival direction, and composition can be inferred.

For solar origin CRs, their detection is possible using satellites at the top of our atmosphere. However, for the case of CR energies larger than 10^{15} eV, the so-called knee energy of the CR spectrum, the flux is extremely low. Such a low flux of CRs can be detected by experiments covering huge surface areas to increase the chance of CRs arriving. The main idea is that when CRs arrive at our atmosphere they collide with molecules in the atmosphere such as oxygen and nitrogen. By these interactions, primary particles (CRs) pro-

duce secondary particles induced by scattering and decay. This is called a cascade or air shower (see Figure 1.1) of secondary particles and covers a huge area of order kilometers. Air showers are widely used to investigate the arrival directions of CRs. Also, they provide very important information about the composition of CRs, whether heavy or light elements such as Fe or P. This can be estimated from air shower properties such as the air shower maximum depth X_{max} . In this manner, air showers provide the energy and composition of CRs by indirect detection.

2. How are Cosmic Rays Accelerated to such Extreme Energies?

Figure 1.2 displays the CR power-law distribution. It shows that CRs arrive with a variety of energies. The distribution indicates the important fact that the acceleration site below the knee is the same as SNRs. Actually, for the lowest energies, they are very common and continuously penetrate us. This particle's origin is known to be the Sun. Most low-energy particles cannot penetrate due to the magnetic field of Earth's atmosphere. Particles in the intermediate range of CR energies, around what is called the knee of the spectrum, are called Very-High-Energy Cosmic Rays (VHECR). The nature and origin of Ultra-High-Energy Cosmic Rays (UHECRs) with energies above $\sim 10^{18}$ eV, at the so-called ankle of the spectrum, are outstanding problems of modern physics.

Many studies have been performed to unravel the problems: where do UHECRs come from, what is the composition of UHECRs, and how are UHECRs accelerated to such extreme energies? UHECRs are believed to be the result of extremely powerful cosmic phenomena (A.M. Hillas (1984)); the most powerful astrophysical events, such

as active galactic nuclei (AGN) (P.L. Biermann (1987)), gamma ray bursts (GRBs) (E. Waxman (1995)), and shock waves around clusters of galaxies (H. Kang et al., (1996)), have been suggested as possible sources of UHECRs. Yet, the nature and origin of UHECRs remain unsolved. See (V. Berezhinsky et al. (2006); K. Kotera et al. (2011)) for reviews.

3. Where do Cosmic Rays Come From?

Cosmic rays (CRs) do not travel in straight lines in space. Their trajectories are bent by intergalactic and interstellar magnetic fields that are known to exist between galaxies and stars. For this reason, even though we may guess their arrival directions at Earth, we do not know exactly where they come from.

Actually, if we can precisely explain the mechanism of how CRs are accelerated to extreme energies, we may guess the source of where the particles are accelerated. Indeed most GCRs are accelerated in SNRs (precisely from supernova explosions) by blast waves. Propagating shock waves interact with turbulent magnetic fields in the well-known mechanism of DSA in which particles bounce back and forth in the turbulent magnetic fields and randomly gain or lose their energy. From this process, cosmic rays are eventually generated. In this manner, CRs reach the high-energy knee and can no longer be contained. Finally, particles escape from their acceleration site, and propagate through the Galaxy. The escaping particle information provides the very important message that CRs leave SNR and can not also accelerate above a certain maximum energy. It also depends on the size of the acceleration site and the age of the object. Much research has reported on this, and that hints on these particles origins and mechanisms are hidden in extragalactic sources.

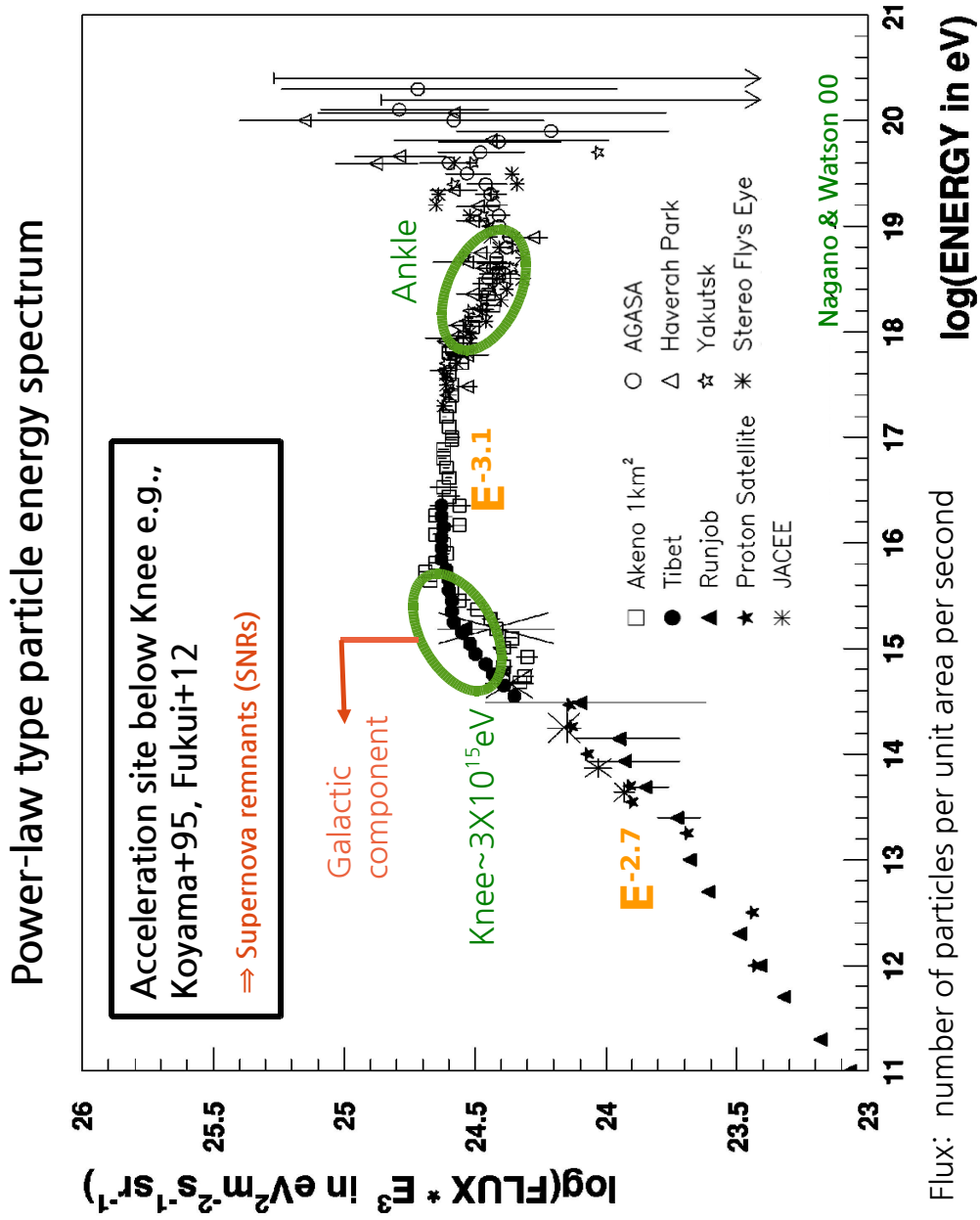


Figure 1.2: Cosmic ray energy distribution that obeys a power-law type. It is obtained by various direct measurements above the atmosphere by air shower detectors.

1.2 Basic Properties of the Interstellar Medium

1.2.1 Overview of the Interstellar Medium (ISM)

The interstellar medium (ISM) is mainly confined to the Galactic disk and is comprised of the gas and dust between stars. From spectroscopy, the chemical compositions of stars consist of approximately 90% Hydrogen, less than 10% Helium, and the remainder of other elements. The chemical composition of the ISM is almost similar to that of stars. The most abundant components of the ISM are dominated by hydrogen which is thought to contribute 90% by number and 70% by mass to a typical interstellar environment. Also, less than 10% of matter consists of He, dust (silicates or carbonaceous material), radiation, magnetic fields, X-rays, and Cosmic Rays (CRs). The regions classified by the state of hydrogen are ionized atomic hydrogen (HII), neutral atomic hydrogen (HI), and molecular hydrogen (H₂).

The typical ISM has a magnetic field strength of a few μG and constrains the motion of primary CRs protons. The ISM is an extremely faint plasma, and even the densest regions are close to a vacuum relative to Earth. The ISM is far from thermal equilibrium and not uniform in our Galaxy. Interstellar clouds are considered as denser-than-average regions, and they can collapse due to mutual gravitational collapse of the gas into stars. Stars form due to molecules and dust enabling gas to cool by converting thermal energy to radiation. By radiation cooling, the ISM can collapse and form stars.

Stars end their lives by returning gas to the ISM. They lose their

mass and can blow most of the ISM out of the Galaxy. This emitted matter contributes to a huge increase in gas density from the typical ISM density of 1 hydrogen atom per cm^{-3} to stellar densities larger than 10^{23} cm^{-3} . The interstellar medium is detected near the spiral disk of the Galaxy, where there are many young stars and clouds. From this, we can determine the structure of the Galaxy from the gas in the interstellar medium. The ISM is very important in astrophysics because interactions between stars and the ISM determines how the Galaxy consumes gas. That is, the ISM controls star formation.

In general, the ISM has a wide range of structures, from < 1 pc to larger than 10^3 pc, with a wide range of densities, $10^{-3} - 10^7$ atoms/ cm^3 , and temperatures, $10 - 10^7$ K. Magnetic fields are generally stronger in denser regions.

The Composition of the Interstellar Medium

1. Interstellar Dust: Dust plays a role in extinction, general obscuration, interstellar reddening, polarization, absorption, and reflection in the ISM. Dust grains are important in the chemistry of the ISM, regulating the formation of molecules. The typical interstellar dust density is 1 per 10^6 m^3 . The total dust mass is 1% of the ISM. In visible light, this dust effectively shields radiation incoming from large distances. For the study of high-density interstellar clouds we need to use infrared and radio wavelengths.

2. Interstellar Gas

I will explain the physical properties of interstellar gas, which has most of the mass of the ISM. Interstellar gas has emission or absorption lines that depends on the gas species. That is, line emission is

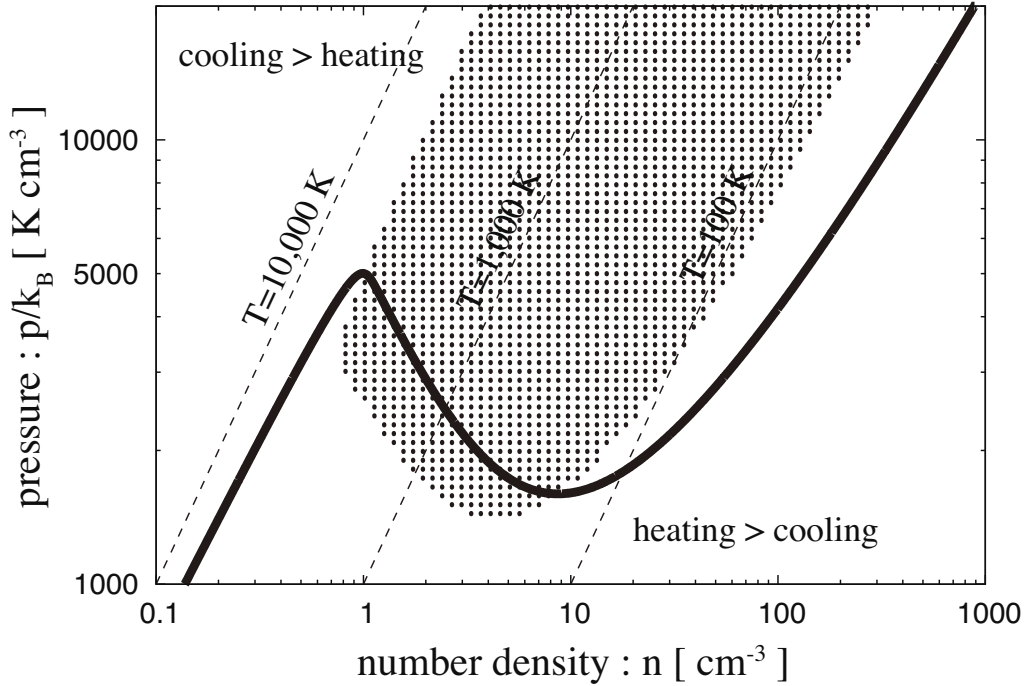


Figure 1.3: Thermal Equilibrium Curve from T. Inoue et al. (2012). The curve indicates the equilibrium condition, $L = 0$.

dependent on the temperature and density of gas. The first observations of the ISM were done in the early 20th century. They discovered relatively broad absorption lines that are related to the atmospheres of stars.

Thermal Equilibrium Curve

The interstellar medium (ISM) is an inhomogeneous, multiphase system in which gases of different temperatures, densities, and ionization fractions can coexist approximately in pressure equilibrium. Because of radiative cooling and heating, it is considered an open system.

In Figure 1.3, $T = 10^2$ K indicates interstellar clouds (cold clouds),

and $T = 10^4$ K indicates diffuse intercloud gas (hot gas). It shows that cold clouds and hot gas are in a thermally unstable equilibrium. Figure 1.3 provides the equilibrium curve (thick solid line), and we can see that below the equilibrium curve cooling is stronger than heating, i.e., cooling is dominant, whereas above the curve heating dominates cooling. This demonstrates that thermal instability in a multiphase medium is believed to be a formation mechanism of cold clouds generated by suppressing cooling. Field et al. (1969) and Wolfire et al. (1995) provides linear stability analyses of the fluid equations with radiative cooling. As a result, they obtained the isobaric criteria for instability.

$$\left. \frac{\partial P}{\partial \rho} \right)_{L=0} \leq 0 \quad (1.1)$$

where, ρ is gas density, P is pressure and L is generalised loss function.

$$L(\rho, T) = \rho^2 \Gamma(T) - \rho G \quad (1.2)$$

where, T is temperature, a cooling rate per unit volume of $\rho^2 \Gamma(T)$, and a heating rate per unit volume of ρG . $L > 0$ is net cooling, $L < 0$ is net heating and $L = 0$ is equilibrium. Therefore, the ISM consists of a complex two-phase structure and is referred to as a multiphase medium. In the ISM, the cold neutral medium (CNM) is very fragmented and turbulent and maintained by interaction with the warm neutral medium (WNM).

1.2.2 Global ISM Models: Five Phases of the ISM

Five phases: (Mihalas & Binney (1981); Kulkarni & Heiles (1988))

The ISM is described physically in terms of its thermodynamic properties: density, temperature, and pressure. In particular, the idea of thermal phases is an important element of this description. The ISM is a system that is very far from thermal equilibrium. Four principal forms of equilibria are encountered: kinetic, excitation, ionization, and pressure.

A stable balance of heating and cooling at a given pressure can often be achieved at more than one temperature. Hence, the multiphase structure of the ISM develops. The thermal pressure in the local disk of the Galaxy is $P/k = nT \sim 2000 - 6000 \text{ cm}^{-3}\text{K}$, about the same order of magnitude as the pressure due to magnetic fields, since turbulence tends to produce an equipartition of the two. Matter is in constant flux between the phases.

	Typical T (K)	Volume Density n cm ⁽⁻³⁾	Volume Filling Factor f (%)
MM	~ 20	> 10 ³	< 1
CNM	~ 100	~ 20-60	~ 2-4
WNM	6000-10000	~ 0.3	30-60
WIM	~ 8000	~ 0.3	≥ 15
HIM	~ 10 ⁶	~ 10 ⁻³	≤ 50

1. The Molecular Medium (MM) : The MM accounts for 30-60% of the total mass of the Galactic ISM due to its high density of $> 10^3 \text{ cm}^{-3}$. These cold dense clouds are bounded mostly gravitationally. On average this phase has large amount of mass but its filling factor is small. It may form stars by unstable gravitational collapse.

HI

2. The Cold Neutral Medium (CNM): The CNM is distributed in dense sheets and filaments. It is mostly composed of neutral hydrogen (HI) in absorption and is not gravitationally bound.

3. The Warm Neutral Medium (WNM): The WNM is traced by HI 21 cm emission. This phase is located mainly in photo-dissociation regions. In the regions surrounding HII regions (WIM; see below) its density may be higher due to considerable heating. Very soft X-rays induce ionization.

HII

4. The Warm Ionized Medium (WIM): The WIM is associated with HII regions in which gas is photo-ionized by hot young stars (Reynolds (1984)). Ionization occurs due to hot B stars.

5. The Hot Ionized Medium (HIM): The hot gas that is heated by strong shocks from supernova explosions or violent stellar winds has a large cooling time. Consequently it can occupy a large fraction of the ISM. In the mid-plane of the Galaxy, HIM is confined within giant shell HII regions and has a small filling fraction. It has a large pressure, and it can be detected by diffuse soft X-ray emission.

Why is the ISM not in thermal equilibrium? Thermal equilibrium requires detailed balance, i.e., each process occurs as often as the inverse process. This is often not true in the ISM. For example, collisional excitation is followed by radiative decay due to low density. There is not always pressure equilibrium because of SN shocks penetrating into the ISM. Dense phases include Giant Molecular Clouds (GMCs) and HII regions. Then, what kind of distributions are valid in the ISM?

The diffuse phases are low density and fill a large fraction of the ISM volume. The molecular material is confined to molecular clouds due to gravitation. These cold, warm, and hot phases are in pressure equilibrium. The ISM phases are in approximate pressure equilibrium as follows:

$$P/k = nT \sim 3000 \text{ cm}^{-3}K, \quad (1.3)$$

$$P_{CNM} \sim P_{WIM}. \quad (1.4)$$

1.3 Cosmic-Ray Acceleration and Observations of Gamma Ray

Cosmic rays are astrophysical energetic particles. Their composition mainly consists of relativistic protons/nuclei. From the results of many studies, possible production sites of CRs are as follows:

- 1) **Galactic:** Supernova Remnants, Compact Objects
- 2) **Extragalactic:** Active Galaxies, Gamma Ray Bursts

SNRs are the most promising cosmic rays accelerators up to the knee. However, we still do not understand how they can reach such extremely high energies. In general, rapidly expanding SNRs have a maximum radius of about $\sim 10^{17}$ m. Because of SNR expansion into interstellar space, a plasma shock is magnetized and causes shock-scattering of particles. This was already referred to in the previous section as Diffusive Shock Acceleration (DSA). From this shock acceleration, the average fractional energy gained at each crossing becomes $\Delta/\epsilon = \beta$. In general, the CR differential spectrum is $n(\epsilon) \sim \epsilon^{-2}$, and allowing for propagation matches the observed spectrum $\sim \epsilon^{-2.7}$.

The main mechanism to convert the kinetic energy generated by Supernova expansion can be described by DSA:

1. First order Fermi acceleration occurs due to head-on collisions:

$$\Delta\epsilon \sim V/c; \tag{1.5}$$

2. Second order Fermi acceleration occurs due to head-on collisions and following the initial collision:

$$\Delta\epsilon \sim (V/c)^2. \tag{1.6}$$

Detection of High-Energy Particles, X-rays, and Gamma Rays : Pion-Decay gamma ray Observations

In general, GeV-TeV energy pion-decay gamma rays are emitted from protons. In particular, the origin of GeV gamma rays is usually explained by the decay of neutral pions produced by accelerated protons (CRs) (Y. Ohira et al.(2011)):

$$\frac{dN}{d\varepsilon} = N(\varepsilon) = \kappa\varepsilon^{-s}. \quad (1.7)$$

The detection method is indirect. In general, 100 GeV gamma rays from decaying pions are produced in hadronic interactions. Of these relativistic particles, only the Galactic Cosmic Rays can be directly detected using spectrometry or a special type of scintillation on a satellite platform on the ground (a so-called surface detector).

Actually, very high-energy electrons are visible through electromagnetic radiation. These electrons can produce synchrotron radiation when they spiral around magnetic fields, inverse Compton (IC) radiation when they collide with low-energy photons, and Bremsstrahlung (also called free-free radiation). These processes (synchrotron, IC, and Bremsstrahlung) produce continuum radiation. Also, relativistic nuclei experience the same processes, however they are heavily suppressed because of the intensity of the electromagnetic radiation from other ions or photons. In principle, photons (here gamma rays) are generated from energetic protons through hadron-hadron or hadron-photon collisions:

$$p + N \rightarrow p + N + \pi^0 \quad (1.8)$$

$$p + \gamma \rightarrow p + \pi^0 \quad (1.9)$$

$$\pi^0 \rightarrow 2\gamma \tag{1.10}$$

where π^0 is a neutral pion and the gamma rays carry away 10% of the proton energy. Recent observations of young SNRs with the HESS Gamma Ray array reported pion signatures near SNRs (Fukui et al. (2012)). It can be believed that CRs protons are accelerated and escape from the area.

In addition to neutrino processes, high-energy neutrinos are believed to be conclusive proof that hadrons as well as electrons are accelerated in SNRs by purely leptonic models. This model ignores relativistic hadrons and assumes they do not produce any relativistic neutrinos.

Cosmic ray protons accelerated by SNRs can penetrate high-density cold cloud regions. Because proton-proton interactions can occur frequently in the ISM, observations can detect more enhanced gamma ray emission produced by pion decay. Indeed, from the gamma ray observations, SNRs interacting with clouds can be brighter (luminous SNRs). Also, the escaping CR protons from SNRs emit gamma rays from the shell of the SNRs and its emission spectrum becomes softer than that from inside SNRs because energy depends on the diffusion of CRs. Therefore, the escape mechanism of CRs from SNRs is very important in modifying the CR spectrum. Also, we need to emphasize that the escape of CRs from SNRs depends on the determination and evolution of the maximum energy of CRs accelerated in the SNRs.

Nevertheless, to know the origin of pion-decay gamma rays has been difficult because high energy (relativistic) electrons can produce gamma rays through bremsstrahlung and Inverse Compton (IC) scattering mechanisms in the so-called leptonic model, (Ackermann et al.

(2013)). According to X-ray observations, relativistic electrons are accelerated to relativistic energies by shock mechanisms in SNRs (K. Koyama et al. (1995)). Therefore, GeV-TeV emission from IC scattering by relativistic electrons or neutral pion decay produced by inelastic collisions between relativistic protons and ambient thermal nuclei can be a crucial key for the origin of CRsn, particle acceleration mechanisms, and neutrino emission from SNRs.

Chapter 2

Dynamics of the Interstellar Medium

2.1 Magnetohydrodynamics (MHD)

Overview

Most baryonic matter in the universe is in the form of plasma (> 99%). Plasma properties include collective behaviour, wave propagation, dispersion, diamagnetic behaviour, Faraday rotation, and so on. A plasma is an ensemble of electrically-charged particles, electrons, ions, and neutral particles. Its collective behaviour is the result of long-range Coulomb forces.

The plasma criteria are as follows:

1. Macroscopic neutrality: Net charge = 0;
 $L \gg \lambda_D$ for collective behaviour, where λ_D is the Debye length and L is size of system;
2. Many particles within the Debye sphere: $N_D \sim n_e \lambda_D^3 \gg 1$;

3. Many plasma oscillations between ion-neutral damping collisions:
 $\omega\tau_{em} \gg 1$;
4. Quasi-neutral plasma.

A requirement is $\lambda \ll l \ll L$, where L is the physical volume, l is the test volume, and λ is the mean free path. Also, the net charge is zero. Magnetic Fields (MFs) are ubiquitous in the universe. The sources of MFs are electric currents, \mathbf{j} . In the ISM the conductivity σ is high, thus large-scale electric fields are negligible and

$$\mathbf{j} = \frac{c}{4\pi}(\nabla \times \mathbf{B}). \quad (2.1)$$

Quantities are characterized by a distribution function in phase space,

$$f_i(\mathbf{x}, \mathbf{p}, t), \quad (2.2)$$

evolving by the Boltzmann equation. MHD is a macroscopic theory marrying Maxwell's equations with the fluid dynamics equations to describe magnetofluid dynamics. Moving charges produce currents that interact with MFs and create a back-reaction on fluid motion.

2.2 Approximations of Magnetohydrodynamics

Mean free path for neutral atoms and molecules

If the mean free path l is much smaller than the macroscopic length scale L , gas particles can be treated as a continuum. Let us define a fluid element (ϵ) and a mean free path (l) is smaller than L . This means that the number of particles in the fluid element is very large.

The velocity of individual particles can be considered as follows:

$$\bar{\mathbf{v}} = \bar{\mathbf{u}} + \bar{\mathbf{w}} \quad (2.3)$$

$$\bar{\mathbf{u}} \equiv \langle \bar{\mathbf{v}} \rangle \quad (2.4)$$

where $\bar{\mathbf{u}}$ is mean (or bulk) velocity and $\bar{\mathbf{w}}$ is random velocity.

If the collision frequency μ is smaller than the gyrofrequency Ω , $\mu \ll \Omega$, then this is considered to be collisionless. In such an environment the gyroradius is much smaller than the variation length scale of \mathbf{E} and \mathbf{B} , and Ω^{-1} is much smaller than the timescale of these field changes. For a neutral atom or molecule the mean free path is

$$l = \frac{1}{n\sigma}, \quad (2.5)$$

$$Volume = \sigma nl = 1, \quad (2.6)$$

where n is the number density and σ is the scattering cross section. Typically, $\sigma \sim 10^{-15} \text{ cm}^2$ for an atomic hydrogen gas cloud ($n \sim 10 \text{ cm}^{-3}$), which yields a mean free path of $l \sim 10^{14} \text{ cm}$. The size of a neutral atom is $1\text{\AA} = 10^{-8} \text{ cm}$.

We now explain conduction in fluids. \mathbf{B} promotes a current in a moving conducting fluid. This current can impart a force to the fluid, and it can also transform \mathbf{B} . Here, we consider a collisionless plasma. We investigate ideal *magnetohydrodynamics* (*MHD*). This means there is so little resistivity ($\sigma \rightarrow \infty$) that we can consider the fluid to be a perfect conductor. In other words, the Reynolds number is very large. Thus, the fluid is bound to the magnetic field since it is a perfect conductor. The ideal MHD equations consist of the continuity equation, the momentum equation, Ampere's law neglecting displacement current ($\partial \mathbf{E} / \partial t$), and the energy conservation

equation.

Maxwell's equations are given by:

$$\nabla \cdot \mathbf{E} = 4\pi\rho_e \quad (2.7)$$

$$\nabla \times \mathbf{E} = -\frac{1}{c} \frac{\partial \mathbf{B}}{\partial t} \quad (2.8)$$

$$\nabla \cdot \mathbf{B} = 0 \quad (2.9)$$

$$\nabla \times \mathbf{B} = \frac{4\pi}{c} \mathbf{J}_e + \frac{1}{c} \frac{\partial \mathbf{E}}{\partial t} \quad (2.10)$$

where $\frac{1}{c} \frac{\partial \mathbf{E}}{\partial t}$ is displacement current, $\mathbf{J}_e = \rho_e \mathbf{v}_e$ is electric current density, and ρ_e is electric charge density.

In an MHD environment, there are four approximations as follows.

1st approximation : $\mathbf{E} \ll \mathbf{B}$

The displacement current is negligible, that is we can ignore the displacement of \mathbf{E} . i.e. $\frac{\partial \mathbf{E}}{\partial t}$. In a non-relativistic environment $v \ll c$, and for small v/c :

$$\frac{E}{B} \sim \frac{v}{c} \ll 1 \quad (2.11)$$

$$E \sim \frac{v}{c} B \quad (2.12)$$

$$E \ll B \quad (2.13)$$

in the laboratory frame.

2nd approximation : $\rho = 0$ and $\mathbf{J}_e \neq 0$.

The total charge density can be written in the form

$$\rho_e \equiv Zen_i - en_e = 0. \quad (2.14)$$

This implies charge neutrality. The total electric current density \mathbf{J}_e is defined by

$$\mathbf{J}_e \equiv Zen_i\mathbf{u}_i - en_e\mathbf{u}_e = -en_e\mathbf{v}'_e \neq 0 \quad (2.15)$$

$$\mathbf{v}'_e \equiv \mathbf{u}_e - \mathbf{u}_i. \quad (2.16)$$

Since $\mathbf{J}_e \neq 0$, Ampere's law becomes $\nabla \times \mathbf{B} = (4\pi\mathbf{J}_e)/c$.

3rd approximation:

In the rest frame, the ion mass is heavy. That is, the electron velocity in the co-moving frame (represented by a prime, ') is the same as the ion velocity in the rest frame. In the case of ideal MHD, $J_e = J'_e$ because the velocity difference between ions and electrons is independent of the frame. Ohms' law is given by

$$\mathbf{J}'_e = \sigma \mathbf{E}', \quad (2.17)$$

where σ is the conductivity. By Lorentz transformation:

$$\mathbf{E}' = \mathbf{E} + \left(\mathbf{v} \times \frac{\mathbf{B}}{c}\right), \quad (2.18)$$

therefore,

$$\mathbf{J}_e = \mathbf{J}'_e = \sigma \left(\mathbf{E} + \mathbf{v} \times \frac{\mathbf{B}}{c}\right). \quad (2.19)$$

Here $\sigma \rightarrow \infty$ and $\mathbf{J}'_e \neq 0$, therefore

$$\mathbf{E} + \left(\mathbf{v} \times \frac{\mathbf{B}}{c}\right) = 0. \quad (2.20)$$

Note that $\eta = c^2/(4\pi\sigma)$. For the ideal MHD case, $\sigma \sim \infty$ so $\eta = 0$ and we have $\sigma \propto \omega_{pe}^2$.

4th approximation: Between the rest frame of ions (primed) and the laboratory frame (unprimed) we have:

$$\mathbf{B}' = \mathbf{B} - (\mathbf{v} \times \frac{\mathbf{E}'}{c}). \quad (2.21)$$

$$(2.22)$$

Therefore we obtain

$$\mathbf{B}' = \mathbf{B}, \quad (2.23)$$

$$\mathbf{E}' = \mathbf{E} + (\mathbf{v} \times \frac{\mathbf{B}}{c}). \quad (2.24)$$

2.2.1 Ideal MHD Equations

We investigate ideal *Magnetohydrodynamics* (*MHD*). MHD is concerned with the dynamics of electrically conducting fluids in the presence of a magnetic field B . MHD assumes there is so little resistivity ($\sigma \rightarrow \infty$) that we can consider the fluid to be a perfect conductor. We consider all dissipative process to be negligible for an ideal fluid, *i.e.*,) there is no viscosity.

In other words, the Reynolds number ($R_M = VL/\eta c/4\pi$) is very large. Thus, the fluid is bound to the magnetic field since it is a perfect conductor.

The ideal MHD equations consist of the continuity equation, the momentum equation, Ampere's law neglecting displacement current ($\partial \mathbf{E}/\partial t$), and the energy conservation equation.

The **Ideal MHD Equations** are given by:

$$\nabla \cdot \mathbf{B} = 0 \quad (2.25)$$

$$\frac{\partial \mathbf{B}}{\partial t} = \nabla \times (\mathbf{v} \times \mathbf{B}) \quad (2.26)$$

$$\frac{\partial \rho}{\partial t} + \nabla \cdot (\rho \mathbf{v}) = 0 \quad (2.27)$$

$$\frac{\partial \mathbf{v}}{\partial t} + (\mathbf{v} \cdot \nabla) \mathbf{v} = -\frac{1}{\rho} \nabla P - \frac{1}{4\pi\rho} \mathbf{B} \times (\nabla \times \mathbf{B}). \quad (2.28)$$

1. The Field Equations of MHD

1.) From Faraday's law,

$$\frac{\partial \mathbf{B}}{\partial t} = -\nabla \times \mathbf{E}, \quad (2.29)$$

$$\nabla \cdot \frac{\partial \mathbf{B}}{\partial t} = -\nabla \cdot (\nabla \times \mathbf{E}), \quad (2.30)$$

$$\frac{\partial}{\partial t} (\nabla \cdot \mathbf{B}) = 0. \quad (2.31)$$

2.) The induction equation describing the evolution of magnetic field is given by

$$\frac{\partial \mathbf{B}}{\partial t} + \nabla \times (\mathbf{B} \times \mathbf{v}) = -\nabla \times (\eta \nabla \times \mathbf{B}), \quad (2.32)$$

with initially

$$\nabla \cdot \mathbf{B} = 0. \quad (2.33)$$

3.) The conservation of electric charge is expressed by

$$\frac{\partial \rho_e}{\partial t} + \nabla \cdot \mathbf{J}_e = 0, \quad (2.34)$$

where ρ_e and \mathbf{J}_e are the electric charge density and electric current density, respectively.

2. The Influence of Magnetic Field on the Fluid

In the lab frame (expressed per particle):

$$\mathbf{f}_i = Ze_i(\mathbf{E} + \frac{\mathbf{v}_i \times \mathbf{B}}{c}), \quad (2.35)$$

$$\mathbf{f}_e = -e_i(\mathbf{E} + \frac{\mathbf{v}_e \times \mathbf{B}}{c}), \quad (2.36)$$

$$\begin{aligned} \mathbf{F} = n_i \mathbf{f}_i + n_e \mathbf{f}_e &= Zen_i(\frac{\mathbf{v}_i}{c} \times \mathbf{B}) - (en_e \frac{\mathbf{v}_e}{c} \times \mathbf{B}) = \\ &= \frac{1}{c}(Zen_i \mathbf{v}_i - en_e \mathbf{v}_e) \times \mathbf{B} = \frac{\mathbf{J}_e \times \mathbf{B}}{c}. \end{aligned} \quad (2.37)$$

The Lorentz force is expressed per volume, and the \mathbf{E} terms have vanished. In Equation. 2.37,

$$\begin{aligned} \mathbf{F} = \frac{\mathbf{J}_e \times \mathbf{B}}{c} &= \frac{1}{4\pi}(\nabla \times \mathbf{B}) \times \mathbf{B} = \\ &= \frac{1}{4\pi}(\mathbf{B} \cdot \nabla)\mathbf{B} - \frac{1}{8\pi}\nabla(|\mathbf{B}|^2), \end{aligned} \quad (2.38)$$

the first term represents magnetic tension due to field lines, and the second term represents magnetic pressure.

2.2.2 MHD Waves: Alfvenic and Magnetosonic Waves

We consider small linear perturbations in waves in a homogeneous conducting medium in a uniform, constant magnetic field \mathbf{B}_0 . The unperturbed medium is homogeneous, *i.e.*, it is also entropic (entropy $S = constant$).

In a static background:

$$\rho_0 = constant, \quad (2.39)$$

$$\mathbf{v}_0 = \mathbf{v}', \quad (2.40)$$

$$P_0 = \text{constant}, \quad (2.41)$$

$$\mathbf{B}_0 = \text{constant}, \quad (2.42)$$

$$\mathbf{B} = \mathbf{B}_0 + \mathbf{B}', \quad (2.43)$$

$$\rho = \rho_0 + \rho', \quad (2.44)$$

$$P = P_0 + P', \quad (2.45)$$

where \mathbf{v}' is also very small value like the perturbed components \mathbf{B}' , ρ' , and P' . Then we apply the above equations to the ideal MHD equations and keep terms up to first order. We consider the flow to be isentropic.

Therefore:

$$P' = u_0^2 \rho', \quad (2.46)$$

$$u_0^2 = \left(\frac{\partial P}{\partial \rho} \right)_s. \quad (2.47)$$

We obtain simple linearized MHD equations:

$$\nabla \cdot \mathbf{B}' = 0, \quad (2.48)$$

$$\frac{\partial \mathbf{B}'}{\partial t} = \nabla \times (\mathbf{v} \times \mathbf{B}'), \quad (2.49)$$

$$\frac{\partial \rho'}{\partial t} + \rho' \nabla \cdot \mathbf{v} = 0, \quad (2.50)$$

$$\frac{\partial \mathbf{v}}{\partial t} = -\left(\frac{u_0^2}{\rho}\right) \nabla \rho' - \frac{(\mathbf{B} \times (\nabla \times \mathbf{B}'))}{4\pi\rho}. \quad (2.51)$$

Small perturbations are considered to be plane waves proportional to $e^{i(\mathbf{k} \cdot \mathbf{r} - \omega t)}$. Hence, the linearized MHD equations become as follows:

$$\omega \mathbf{B}' = \mathbf{k} \times (\mathbf{v} \times \mathbf{B}), \quad (2.52)$$

$$\omega \rho' = \rho \mathbf{k} \cdot \mathbf{v}, \quad (2.53)$$

$$-\omega \mathbf{v} + \left(\frac{u_0^2}{\rho}\right) \rho' \mathbf{k} = -\mathbf{B} \times (\mathbf{k} \times \mathbf{B}'), \quad (2.54)$$

with $\nabla \cdot \mathbf{B}' = 0$.

Thus, $\mathbf{k} \cdot \mathbf{B}' = 0$, so from $\omega \mathbf{B}' = \mathbf{k} \times (\mathbf{v} \times \mathbf{B})$, we obtain $\mathbf{B}' \perp \mathbf{k}$. Using the phase velocity $v_{ph} = \omega/k$, we rewrite the result in component form:

$$v_{ph} B'_z = -v_z B_x, \quad (2.55)$$

$$v_{ph} v_z = -\frac{B_x B'_z}{4\pi\rho}. \quad (2.56)$$

From Equations. 2.55 and 2.56, we obtain the Alfven velocity:

$$v_{ph} = \frac{|B_x|}{\sqrt{4\pi\rho}} \equiv v_{alfven}. \quad (2.57)$$

B'_z is perpendicular to the direction of propagation and constant field \mathbf{B} oscillations, and thus

$$v_z = -\frac{B'_z}{\sqrt{4\pi\rho}}. \quad (2.58)$$

Therefore, the direction of v_z is opposite to B'_z . Eventually, from Equation. 2.58, we can obtain the dispersion relation:

$$\omega = \frac{\mathbf{B} \cdot \mathbf{k}}{\sqrt{4\pi\rho}}. \quad (2.59)$$

If \mathbf{B} and \mathbf{k} are in the same direction, we can obtain $v_{ph} = v_{alfven}$. The physical velocity of the propagation of waves is called the "**group velocity**",

$$\mathbf{v}_{group} = \frac{\partial\omega}{\partial\mathbf{k}} = \frac{\mathbf{B}}{\sqrt{4\pi\rho}}, \quad (2.60)$$

where ω is the angular frequency of waves, usually expressed in radians per second, and \mathbf{k} is the angular wave number of wave, expressed in radians per meter. Group velocity does not involve the direction

of \mathbf{k} . Wave energy propagates with v_{group} . The direction of wave propagation is in the direction of its group velocity and the direction of \mathbf{B} . We consider the propagation of small disturbances in a homogeneous conducting medium in a uniform, constant magnetic field \mathbf{B}_0 . *i.e.*, $\mathbf{B}_0 = constant$. For ideal fluids we neglect all dissipation processes.

Chapter 3

Acceleration of Cosmic Rays

3.1 Cold Plasma

3.1.1 Introduction to Cold Plasma

We consider the plasma as a cold magnetofluid with an associated dielectric constant. We derive a wave equation using Maxwell's equations. Assuming a harmonic solution will then give a dispersion relation that describes all possible propagating wave modes consistent with our assumptions. The characteristics of plasma wave propagation can be used to diagnose the medium. A cold plasma is regarded as having waves that propagate through the plasma much faster than the typical thermal velocity:

$$v_p \gg v_{th} = \sqrt{2k_b T/m}, \quad (3.1)$$

$$c_s \propto \sqrt{P/\rho} \approx 0. \quad (3.2)$$

3.1.2 Wave Equations

To study plasma waves accounting for two-fluid effects, we can start by deriving a very general wave equation that deals with weak waves in a homogeneous plasma with or without a magnetic field. It also governs electromagnetic waves for other dielectric media. Here, the wave equations and dispersion relation for the wave modes are given relative to the dielectric tensor.

First, we consider a homogeneous neutral plasma. In a homogeneous medium, a general solution can be constructed as a superposition of plane wave solutions. The propagation of small-amplitude waves is described by linearized equations in which other higher-order terms have been omitted, *e.g.*, $\mathbf{u}_1 \times \mathbf{B}_1$.

Subscripts 0 and 1 indicate equilibrium and perturbed quantities, respectively. Assuming small perturbations:

$$n = n_0 + n_1, \tag{3.3}$$

$$\mathbf{u} = \mathbf{u}_1, \tag{3.4}$$

$$\mathbf{E} = \mathbf{E}_1, \tag{3.5}$$

$$\mathbf{B} = \mathbf{B}_0 + \mathbf{B}_1, \tag{3.6}$$

$$n_e = n_i. \tag{3.7}$$

This means there are equal numbers of electrons and ions. Both plasma species are at rest, that is

$$\mathbf{u}_0 = 0 \Rightarrow \mathbf{E}_0 = 0. \tag{3.8}$$

From Ampere's law:

$$\nabla \times \mathbf{B}_0 = \mathbf{J}_0 = 0. \quad (3.9)$$

We start with Maxwell's equations, which we write as

$$\nabla \times \mathbf{E}_1 = \frac{\partial \mathbf{B}_1}{\partial t}, \quad (3.10)$$

$$\nabla \times \mathbf{B}_1 - \frac{1}{c^2} \frac{\partial \mathbf{E}_1}{\partial t} = \mu_0 \mathbf{J}_1 = \mu_0 \Sigma e n_0 \mathbf{u}_1, \quad (3.11)$$

$$\nabla \cdot \mathbf{E}_1 = \frac{q}{\epsilon_0} = \frac{1}{\epsilon_0} \Sigma e n_1, \quad (3.12)$$

$$\nabla \cdot \mathbf{B}_1 = 0. \quad (3.13)$$

Combining Equations. 3.10 and 3.11 to eliminate \mathbf{B}_1 yields

$$\nabla \times \nabla \times \mathbf{E}_1 = -\frac{1}{c^2} \frac{\partial^2 \mathbf{E}_1}{\partial t^2} - \mu_0 \frac{\partial \mathbf{J}_1}{\partial t}. \quad (3.14)$$

Then, substituting $\mathbf{n} = \frac{c\mathbf{k}}{\omega}$ into Equation. 3.14, where \mathbf{n} is refractive index, yields

$$\mathbf{n} \times \mathbf{n} \times \mathbf{E}_1 = -\mathbf{E}_1 - \frac{i}{\epsilon_0 \omega} \sigma \cdot \mathbf{E}_1 = -\kappa \cdot \mathbf{E}_1. \quad (3.15)$$

Here, $\sigma \cdot \mathbf{E}_1 = \mathbf{J}_1$, where σ is the conductivity tensor and a is function of both \mathbf{k} and ω , and $\kappa = \mathbf{I} - \frac{\sigma}{i\omega\epsilon_0}$ is the dielectric tensor.

3.1.3 Cold Plasma Dielectric Permittivity

In a collisionless plasma

$$m_i n \frac{\partial \mathbf{V}}{\partial t} = \mathbf{J}_1 \times \mathbf{B}_0, \quad (3.16)$$

$$\mathbf{E}_1 = -\mathbf{V} \times \mathbf{B}_0 + \frac{\mathbf{J}_1 \times \mathbf{B}_0}{ne} + \frac{m_e}{ne^2} \frac{\partial \mathbf{J}_1}{\partial t}, \quad (3.17)$$

where $\mathbf{V} = \frac{m_e \mathbf{v}_e + m_i \mathbf{v}_i}{m_i + m_e}$. Substitution of the plane wave solution into Equations. 3.16 and 3.17 yields

$$-i\omega m_i n \mathbf{V}_1 = \mathbf{J}_1 \times \mathbf{B}_0, \quad (3.18)$$

$$\mathbf{E}_1 = -\mathbf{V}_1 \times \mathbf{B}_0 + \frac{\mathbf{J}_1 \times \mathbf{B}_0}{ne} - i\omega \frac{m_e}{ne^2} \mathbf{J}_1. \quad (3.19)$$

Eliminating the fluid velocity \mathbf{V}_1 , we obtain

$$-i\omega \epsilon_o \mathbf{E}_1 = \frac{\omega^2 \mathbf{J}_1 - i\omega \Omega_e \mathbf{J}_1 \times \mathbf{b} + \Omega_e \Omega_i \mathbf{J}_\perp}{\omega_{pe}^2}, \quad (3.20)$$

where $\omega_{pe} = \sqrt{\frac{ne^2}{\epsilon_o m_i}}$ is the plasma frequency and $\Omega_i = -\frac{eB_0}{m_i}$ is the cyclotron frequency. The Notation “ i ” can refer to electron or ion. From Equation. 3.20 we can obtain the parallel and perpendicular components. The parallel component is given by

$$\mathbf{J}_\parallel = \frac{\omega_{pe}^2}{\omega^2} (i\omega \epsilon_o \mathbf{E}_\parallel), \quad (3.21)$$

$$\mathbf{J}_\pm = \mathbf{J}_\perp = \frac{\omega_{pe}^2}{\omega^2 \pm \omega \Omega_e + \Omega_e \Omega_i} (i\omega \epsilon_o \mathbf{E}_\pm), \quad (3.22)$$

where $\mathbf{J}_\pm = \mathbf{J} \cdot \mathbf{e}_\pm$. Therefore, from Equations. 3.21 and 3.22, for the parallel case we have

$$\sigma_\parallel = \frac{\omega_{pe}^2}{\omega^2} (i\omega \epsilon_o). \quad (3.23)$$

Eventually we obtain

$$\kappa_\parallel = 1 - \frac{\sigma_\parallel}{i\omega \epsilon_o} = 1 - \frac{\omega_{pe}^2}{\omega^2} = P. \quad (3.24)$$

Using Equation. 3.24, for the perpendicular case we have

$$\sigma_{\pm} = \sigma_{\perp} = \frac{\omega_{pe}^2}{\omega^2 \pm \omega\Omega_e + \Omega_e\Omega_i} i\omega\epsilon_0, \quad (3.25)$$

$$\kappa_{\perp} = \kappa_{+} = \frac{\omega_{pe}^2}{\omega^2 + \omega\Omega_e + \Omega_e\Omega_i} = R, \quad (3.26)$$

$$\kappa_{\perp} = \kappa_{-} = \frac{\omega_{pe}^2}{\omega^2 - \omega\Omega_e + \Omega_e\Omega_i} = L. \quad (3.27)$$

Thus, the dielectric permittivity takes the form

$$\kappa = \begin{pmatrix} R & 0 & 0 \\ 0 & L & 0 \\ 0 & 0 & P \end{pmatrix}.$$

R and L represent the permittivity for right- and left-handed circularly polarized wave permittivity, respectively. Then, the permittivity parallel to the magnetic field, P , is same as for an unmagnetized plasma. In order to obtain the dielectric permittivity in Cartesian coordinates, we can use the unitary matrix U :

$$U = \frac{1}{\sqrt{2}} \begin{pmatrix} 1 & 1 & 0 \\ i & -i & 0 \\ 0 & 0 & \sqrt{2} \end{pmatrix}.$$

Then, the new κ is

$$\kappa = \begin{pmatrix} S & iD & 0 \\ iD & S & 0 \\ 0 & 0 & P \end{pmatrix},$$

where $S = \frac{R+L}{2}$ and $D = \frac{R-L}{2}$ indicate the sum and the difference of the right- and left-handed circularly polarized wave permittivity, respectively.

Now, we obtained the dielectric permittivity in Cartesian coordinates:

$$\mathbf{n} \times \mathbf{n} \times \mathbf{E}_1 = -\mathbf{E}_1 - \frac{i}{\epsilon_0 \omega} \sigma \cdot \mathbf{E}_1 = -\kappa \cdot \mathbf{E}_1. \quad (3.28)$$

This equation can be expressed in the form $\mathbf{M} \cdot \mathbf{E}_1 = 0$. We can get M as follows:

$$m = \begin{pmatrix} S - n^2 \cos^2 \theta & iD & n^2 \cos \theta \sin \theta \\ iD & S - n^2 & 0 \\ n^2 \cos \theta \sin \theta & 0 & P - n^2 \sin^2 \theta \end{pmatrix}$$

The condition for a non-trivial solution is that the determinant of the matrix be zero. *i.e.*,) $M(\omega, k) = An^4 - Bn^2 + C = 0$. This called dispersion relation.

$$A = S \sin^2 \theta + P \cos^2 \theta \quad (3.29)$$

$$B = RL \sin^2 \theta + PS(1 + \cos^2 \theta) \quad (3.30)$$

$$c = PRL \quad (3.31)$$

$$S^2 - D^2 = RL \quad (3.32)$$

where, θ be the angle between \mathbf{k} and \mathbf{B}_0 . If we solve $M(\omega, k) = An^4 - Bn^2 + C = 0$ with n^2 , it follows n^2 is real always. That is n is either purely real or imaginary. Thus, wave is either propagation or decay. From dispersion relation,

$$\tan^2 \theta = -\frac{P(n^2 - R)(n^2 - L)}{(Sn^2 - RL)(n^2 - P)} \quad (3.33)$$

Equilibrium \mathbf{B}_0 is directed along the z direction, wave vector k lines in the x-z plane. Then, there are two principal modes: $\theta = 0^\circ$

or $\theta = 90^\circ$. For the special case of wave propagation parallel to the \mathbf{B}_0 ,

$$P = 0 \text{ or } n^2 = R \text{ or } n^2 = L \quad (3.34)$$

For the special case of wave perpendicular to the \mathbf{B}_0 ,

$$n^2 = \frac{RL}{S} \text{ or } n^2 = R \quad (3.35)$$

3.1.4 Wave Propagation Parallel to the B_0 : $\theta = 0^\circ$

1. Unmagnetized plasma

Let us now investigate the cold plasma dispersion relation in detail. First, we consider the case $\mathbf{B}_0 = 0$. Absent of $\mathbf{B}_0 = 0$, we can assume \mathbf{k} is z direction. Thus, linearized Equation. of motion becomes,

$$m_e \frac{\partial \mathbf{v}_1}{\partial t} = e \mathbf{E}_1 \quad (3.36)$$

Then,

$$m(-i\omega) \mathbf{v}_1 = e \mathbf{E}_1 \quad (3.37)$$

Use this to eliminate \mathbf{v}_1 from Equation. 3.37,

$$\mathbf{v}_1 = \frac{e \mathbf{E}_1}{-im\omega} \quad (3.38)$$

$$\mathbf{J}_1 = \Sigma en_0 \left(\frac{e \mathbf{E}_1}{-im\omega} \right) = \Sigma \frac{n_0 e^2}{(-i\omega)m} \mathbf{E}_1 \quad (3.39)$$

That is,

$$\sigma = \mathbf{I} \Sigma \frac{n_0 e^2}{(-i\omega m)} \text{ because } \mathbf{J}_1 = \sigma \cdot \mathbf{E}_1 \quad (3.40)$$

Using plasma frequency ω_{pe}^2 , we can obtain the dielectric tensor:

$$\kappa_{(\text{un-magnetized})} = \mathbf{I} \left(1 - \frac{\omega_{pe}^2}{\omega^2} \right) \quad (3.41)$$

Note,

$$\omega_{pi}^2 + \omega_{pe}^2 \simeq \omega_{pe}^2 \text{ since } m_e \ll m_i \quad (3.42)$$

We get dispersion relation.

Expression 1) $c^2 \mathbf{k} \times (\mathbf{k} \times \mathbf{E}_1) = -(\omega^2 - \omega_{pe}^2) \mathbf{E}_1$

$$M = \begin{pmatrix} -c^2 k^2 + \omega^2 - \omega_{pe}^2 & 0 & 0 \\ 0 & -c^2 k^2 + \omega^2 - \omega_{pe}^2 & 0 \\ 0 & 0 & \omega^2 - \omega_{pe}^2 \end{pmatrix}$$

or,

Expression 2) expression 1/ ω^2 = expression 2

$$M = \begin{pmatrix} P - n^2 & 0 & 0 \\ 0 & P - n^2 & 0 \\ 0 & 0 & P \end{pmatrix}$$

where,

$$1 - \frac{\omega_{pe}^2}{\omega^2} = P \quad (3.43)$$

Therefore, dispersion relation for un-magnetized case becomes,

$$\mathbf{M}(\mathbf{k}, \omega) = (-c^2k^2 + \omega^2 - \omega_{pe}^2)^2(\omega^2 - \omega_{pe}^2)^2 = 0 \quad (3.44)$$

There are two types of wave.

Case 1) eigen vector $(0, 0, E_{1z})$, then dispersion relation is $P = 1 - \frac{\omega_{pe}^2}{\omega^2} \approx 0$, since $m_e \ll m_i$. This wave has \mathbf{k} parallel to \mathbf{E}_1 and called longitudinal or plasma wave. In this case, it follows from Faraday' law ($\mathbf{k} \times \mathbf{E}_1 = \omega \mathbf{B}_1$) that $\mathbf{B}_1 = 0$. It means that this wave is purely electrostatic since $\omega = \omega_{pe}$. Thus, ω is independent of \mathbf{k} . From this, we can obtain group velocity.

$$v_{group} = \frac{\partial \omega}{\partial \mathbf{k}} = 0 \quad (3.45)$$

This indicates the wave does not propagate.

Case 2) eigen vector $(E_{1x}, E_{1y}, 0)$, then dispersion relations solution show

$$1) \omega^2 = \omega_{pe}^2 + c^2k^2 \quad (3.46)$$

This wave has \mathbf{k} perpendicular to \mathbf{E}_1 and called transverse wave.

$$2) \omega^2 = c^2k^2 \quad (3.47)$$

This wave is known well as vacuum dispersion relation. From this, in order to propagate of this wave, ω should be larger than ω_{pe} .

ω_{pe} is proportional to plasma density. This means that electromagnetic wave will propagate through a plasma when n (refractive index) fall below a critical value.

$$\omega \gg \omega_{pe} \propto \sqrt{n} \quad (3.48)$$

From $\omega^2 = \omega_{pe}^2 + c^2k^2$,

$$k = \pm \frac{1}{c} \sqrt{\omega^2 - \omega_{pe}^2} \quad (3.49)$$

For $|\omega| > \omega_{pe}$, k is real, so this is propagating wave. For $|\omega| < \omega_{pe}$, k is imaginary (ik), so this is exponential decaying wave. This means that non-propagating wave also called evanescent wave.

2. Magnetized plasma

$$m = \begin{pmatrix} S - n^2 & iD & n^2 \\ iD & S - n^2 & 0 \\ n^2 & 0 & P - n^2 \end{pmatrix}$$

There are three solutions.

$$P = 0 \text{ or } n^2 = R \text{ or } n^2 = L \quad (3.50)$$

1) $P = 0$ same as un-magnetized plasma: This case, magnetic field has no effect on this mode since the particle oscillate along magnetic field and $\mathbf{v}_1 \times \mathbf{B}_1$ (force) vanishes.

2) The right handed polarized wave: $n^2 = R$.

$$n_R^2 = 1 - \frac{\omega_{pi}^2}{\omega(\omega + \Omega_{ci})} - \frac{\omega_{pe}^2}{\omega(\omega - \Omega_{ci})} \quad (3.51)$$

3) The left handed polarized wave: $n^2 = L$.

$$n_L^2 = 1 - \frac{\omega_{pi}^2}{\omega(\omega - \Omega_{ci})} - \frac{\omega_{pe}^2}{\omega(\omega + \Omega_{ci})} \quad (3.52)$$

3.1.5 Whistler Waves

$$\omega = 5\Omega = 2.72 \times 10^{-3}\Omega_{ce} \quad (3.53)$$

$$k = k_x = 2.044\Omega_{ci}/V_A \quad (3.54)$$

$$|B_w|/B_0 = 10^{-4} \quad (3.55)$$

$$r_e = (0, 0, 0) \quad (3.56)$$

$$V_e = (V_{ex,0}, V_{e,\perp}\cos\alpha, V_{e,\perp}\sin\alpha) \quad (3.57)$$

$$(V_{ex,0}, \alpha) = (-6000V_A, 6000V_A) \times (0, 2\pi) \quad (3.58)$$

$$V_a = 10^{-4}c \quad (3.59)$$

If n^2 is negative, from the equation

$$n = \frac{\mathbf{k}c}{\omega} \quad (3.60)$$

\mathbf{k} is imaginary. That is wave doesn't propagation. In other hand, If n^2 is positive, there are two waves which have a opposite directions.

In the origin formula, the small mass ratio ordering $\frac{m_e}{m_i} \ll 1$ has already been applied into the cold plasma. We use cyclotron frequency as an absolute value.

1. in case of $\omega \ll \Omega_e$

$$R = 1 - \frac{\omega_{pi}^2}{\omega(\omega + \Omega_i)} - \frac{\omega_{pe}^2}{\omega(\omega - \Omega_e)} \quad (3.61)$$

$$\sim 1 + \frac{\omega_{pi}^2}{\Omega_i(\omega + \Omega_i)} \quad (3.62)$$

$$L = 1 - \frac{\omega_{pi}^2}{\omega(\omega - \Omega_i)} - \frac{\omega_{pe}^2}{\omega(\omega + \Omega_e)} \quad (3.63)$$

$$\sim 1 - \frac{\omega_{pi}^2}{\Omega_i(\omega - \Omega_i)} \quad (3.64)$$

if $v_A \ll c$, $n^2 = R$

$$\omega_R^2 = \frac{k^2 c^2}{1 + \frac{c^2}{v_A} \left(\frac{\Omega_i}{\omega \Omega_i} \right)} \quad (3.65)$$

$$\sim k^2 v_A^2 \left(1 + \frac{\omega}{\Omega_i} \right) \quad (3.66)$$

$$\omega_L^2 = \frac{k^2 c^2}{1 + \frac{c^2}{v_A} \left(\frac{\Omega_i}{\omega \Omega_i} \right)} \quad (3.67)$$

$$\sim k^2 v_A^2 \left(1 + \frac{\omega}{\Omega_i} \right) \quad (3.68)$$

2. in case of $\omega \gg \Omega_e$

$$R = 1 - \frac{\omega_{pi}^2}{\omega(\omega + \Omega_i)} - \frac{\omega_{pe}^2}{\omega(\omega - \Omega_e)} \quad (3.69)$$

$$\sim 1 + \frac{\omega_{pe}^2}{\omega(\omega - \Omega_e)} \quad (3.70)$$

$$L = 1 - \frac{\omega_{pi}^2}{\omega(\omega - \Omega_i)} - \frac{\omega_{pe}^2}{\omega(\omega + \Omega_e)} \quad (3.71)$$

$$\sim 1 - \frac{\omega_{pe}^2}{\omega(\omega + \Omega_e)} \quad (3.72)$$

3. in case of $\omega \ll \Omega_i$

$$\omega + \Omega_i \sim \Omega_i$$

$$R = 1 + \frac{\omega_{pi}^2}{\Omega_i(\omega + \Omega_i)} \quad (3.73)$$

$$\sim 1 + \frac{\omega_{pi}^2}{\Omega_i^2} \quad (3.74)$$

$$L = 1 - \frac{\omega_{pi}^2}{\Omega_i(\omega - \Omega_i)} \quad (3.75)$$

$$\sim 1 + \frac{\omega_{pi}^2}{\Omega_i^2} \quad (3.76)$$

if $v_A \ll c$, $n^2 = R$

$$R \sim 1 + \frac{\omega_{pi}^2}{\Omega_i^2} = 1 + \frac{c^2}{v_A^2} \quad (3.77)$$

$$\omega_R^2 \sim k^2 v_A^2 \quad (3.78)$$

$$\omega_L^2 \sim k^2 v_A^2 \quad (3.79)$$

At low frequency $\omega \ll \Omega_i$ the right and left circularly polarized waves are right and left circularly polarized Alfvén wave.

4. $\Omega_i \ll \omega \ll \Omega_e$

$$\omega + \Omega_e \sim \Omega_e$$

$$R = 1 + \frac{\omega_{pi}^2}{\Omega_i(\omega + \Omega_i)} \quad (3.80)$$

$$L = 1 - \frac{\omega_{pi}^2}{\Omega_i(\omega - \Omega_i)} \quad (3.81)$$

includes $\omega \gg \Omega_i$. $\omega + \Omega_i \sim \omega$. Then

$$R = 1 + \frac{\omega_{pi}^2}{\omega \Omega_i} \quad (3.82)$$

$$L = 1 - \frac{\omega_{pi}^2}{\omega\Omega_i} \quad (3.83)$$

if $v_A \ll c$,

$$\omega_R = \frac{k^2 v_A^2}{\Omega_i} \quad (3.84)$$

$$\omega_L = -\frac{k^2 v_A^2}{\Omega_i} \quad (3.85)$$

5. $\omega \gg \Omega_i$

$$R \sim 1 + \frac{\omega_{pe}^2}{\omega(\omega - \Omega_e)} \quad (3.86)$$

$$L \sim 1 - \frac{\omega_{pe}^2}{\omega(\omega + \Omega_e)} \quad (3.87)$$

$$(3.88)$$

includes $\omega \gg \Omega_e$. $\omega - \Omega_e \sim \omega$. Then

$$R = 1 + \frac{\omega_{pe}^2}{\omega^2} \quad (3.89)$$

$$L = 1 - \frac{\omega_{pe}^2}{\omega^2} \quad (3.90)$$

$$(3.91)$$

if $v_A \ll c$,

$$\omega_R = \frac{k^2 v_A^2}{\omega^2} = 1 \quad (3.92)$$

$$\omega_L = \frac{k^2 v_A^2}{\omega^2} = 1 \quad (3.93)$$

3.2 Resonance of Particles

[Ref. Particle acceleration in astrophysical plasmas By Dennis L. Gallagher]. This section shows the relation between the particle acceleration and plasma waves. We can consider the linear approximation of the equations for weak interaction case. In general, this weak interaction is treated to be occurred resonant interactions. The resonance can be occurred when velocity of particle and wave phase velocity are matched. The resonance condition is considered without a background magnetic field or along the magnetic field, it is described as follows (Davidson, 1972, p 134)

$$\omega_k - \mathbf{k} \cdot \mathbf{v} = 0 \quad (3.94)$$

where ω_k is wave frequency, \mathbf{k} is wave vector, \mathbf{v} is particle velocity. Equation. 3.94 treats for a single wave where the component of the particle velocity along the wave vector satisfies the wave phase velocity. For the particle motions transverse to the magnetic field, the resonance condition is described as follows:

$$\omega' = \omega_k - \mathbf{k}_{\parallel} \mathbf{v}_{\parallel} = n\Omega_c \quad (3.95)$$

Here, number n is an integer, in general, it indicate the harmonics of the particle cyclotron frequency (Ω_c). The resonance condition considers the Doppler shift from the interaction between particle and wave.

3.2.1 Resonance in Unmagnetized Plasma

The resonance between particle and wave is occurred when the resonance condition is matched. This section shows the resonance in a

case of an unmagnetized plasma.

$$\omega_k - \mathbf{k} \cdot \mathbf{v} = 0 \quad (3.96)$$

This equation indicates the resonance condition with particle velocity \mathbf{v} in an unmagnetized plasma. It corresponds to a resonance that when Equation. 3.96 is matched the particles undergo electric field (as static) from the wave in the rest frame of particles. Here, we need to consider a wave with frequency ω and its vector \mathbf{k} in the laboratory frame. Then, we transform the frame from the lab to rest frame by using a Lorentz transformation, it shows the new wave quantities with ω' , \mathbf{k}' in the rest frame as follows:

$$\omega' = \gamma(\omega_k - \mathbf{k} \cdot \mathbf{v}) \quad (3.97)$$

where γ is the Lorentz factor. This equation is same when we consider the fields as static in the rest frame of the particle. That is, $\omega' = 0$ by using Equation. 3.96 in the laboratory frame.

3.2.2 Resonance in Magnetized Plasma

The resonance condition in the magnetic field is the Doppler condition

$$\omega_k - k_{\parallel} v_{\parallel} = n\Omega_c \quad (3.98)$$

where, $\Omega_c = |q|B/m$ is gyrofrequency of particle, and k_{\parallel} , v_{\parallel} are the components of \mathbf{k} and \mathbf{v} parallel to magnetic field (\mathbf{B}). Resonances at $n > 0$ can be explained via the normal Doppler effect. mean free path :

$$l = \frac{1}{n\sigma} \quad (3.99)$$

$$\sigma = a^2\pi \quad (3.100)$$

Thermal velocity

$$V_{th} = \sqrt{\frac{k_B T}{m_e}} \quad (3.101)$$

Atom size is $a = 10^{-8}$ cm since distance is 10^{-10} m.

Particle acceleration provides that in the energy-flux distribution, we can observe the power law distribution. It is different with Maxwellian distribution. If mean free path is shorter than planet rotating time scale, it cannot be occurred the particle acceleration. Particles, normally we say neutral particles, can collide many particles before acceleration. In this case, we just say that it is showed the Maxwell-Boltzmann distribution. This distribution is totally different with power law distribution. To explain the particle acceleration, their distribution is considered important.

Therefore, for planetary disk particle acceleration cannot be occurred. However, pulsar, neutron star case, inside of pulsar cannot be occurred particle acceleration. Because neutron star's particles are combined already, therefore their mean free path is very short. However, outside of pulsar, the density can be considered as zero. Thus, we can see the particle acceleration that point. The point about particle acceleration, it is informant to understand of mean free path. That length scale is whether larger than which scale.

Mean flight time becomes:

$$t_f = \frac{l}{V_{th}} \quad (3.102)$$

For the protoplanetary disk, mean flight time is around 10^{-5} s. 1yr is 1.5×10^8 s. Therefore, in the protoplanetary disk, particle accel-

eration cannot be occurred. This is obviously correct.

The concept of mean flight time is similar to relaxation time. For relaxation time, we normally use in case of plasma. Neutral case, N_2 or O_2 are molecule and their mass case, we can consider that same mass they have. Then, for the collision, only 2 or 3 times, they have got Maxwell-Boltzmann distribution from nearly "perfect elastic collision". However, plasma case it is different issue. The energy of proton and electron are same. However, their mass is different $1842 \times m_e = m_i$. Then, velocity is different factor of ~ 43 . Therefore, Proton is heavier than electron and the velocity slower than electron. Thus, we can say relaxation time of electron is very shorter than proton case. Note) relaxation time between electron and proton is very long because of their column effect (scattering).

c.f) Hillas arguing that in order for it to accelerate CR particles to high energies, the size of the acceleration region must be at least twice the Larmor radius. $C_s = 340$ m/s,

Chapter 4

Numerical Simulations of the Diffusion of Cosmic Rays

4.1 Hydrodynamics Simulations

We perform a study of the escape of CRs from their acceleration sites by diffusion due to interactions with turbulent magnetic fields. We investigate the diffusion of CRs using a hydrodynamics simulation of a strong shock wave propagating in an interstellar medium. In order to quantitatively analyse the diffusion of high-energy CRs, we performed test-particle numerical simulations of CR protons using three-dimensional magnetohydrodynamics (MHD) simulations of T. Inoue et al. (2012) and T. Inoue et al. (2013).

The interstellar medium (ISM) is an open system in which radiative cooling and heating are effective. It is an inhomogeneous, multiphase system in which gases of different temperatures, densities,

and ionization fractions can coexist in approximate pressure equilibrium. Diffuse warm gas (diffuse intercloud gas) with $T \simeq 10^4$ K and HI clouds (interstellar clouds) with $T \simeq 10^2$ K are approximately in pressure equilibrium in a typical ISM environment (see Figure 1.3). As a consequence of thermal instability driven by external compressional events, such as shock waves due to expanding HII regions or very late phase SNRs, unstable gas evolves into diffuse gas and HI clouds (S. Inutsuka et al.(2005); T. Inoue et al. (2008); T. Inoue et al. (2012)). Therefore, inhomogeneities inevitably emerge and remain ubiquitous in the ISM. The characteristic length scale of an inhomogeneity can be expressed in terms of the ‘‘Field length’’, which is the critical wavelength of the thermal instability (K. Koyama et al.(2004); G.B. Field (1965)). The Field length depends on density and temperature and can be smaller than 1 parsec. A blast wave generated by supernova expansion sweeps up dense and clumpy HI clouds of the multiphase ISM, which eventually generates strong velocity shear in magnetic fields. Magnetic fields undergo amplification from their typical strength of μG to mG due to turbulent dynamo processes in the post-shock region (T. Inoue et al.(2010); T. Inoue et al. (2012); T. Inoue et al. (2013); J. Giacalone (2007)). This process may explain the existence of magnetic fields of mG strength which is suggested by Y. Uchiyama et al.(2007). Figure 4.1 shows the time variability of synchrotron X-rays with one year.

1. Description of One-phase Medium Simulation

Simulations of shocked SNRs driven by the Richtmyer-Mechkov instability (RMI) have been performed by T. Inoue et al. (2013) to demonstrate the magnetic field amplification and magnetic field distribution of turbulent SNRs. An initially unperturbed magnetic field

was set up in the (positive) y -direction with strength $5 \mu\text{G}$, considered a typical ISM magnetic field strength (Beck, 2000). Based on this, they investigated the interaction between a strong shock wave ($v_{sh} \sim 1800 \text{ km s}^{-1}$) and interstellar density fluctuations.

They considered an adiabatic gas with adiabatic index $\Gamma = 5/3$. Density fluctuations superposed by sinusoidal functions were included and followed an isotropic power-law spectrum with random phases. The power spectrum of the density fluctuations was shown to be well described by an isotropic power law for wavenumbers k in the inertial range of turbulence, $P(k) = \rho_k^2 k^2 \propto k^{-5/3}$, where ρ_k is the Fourier component of the density. The mean number density and the initial thermal pressure were taken to be $\langle n_0 \rangle = 0.5 \text{ cm}^{-3}$ and $p/k_B = 4 \times 10^3 \text{ K cm}^{-3}$. To induce the blast wave, a hot plasma was set up with $p_h/k_B = 2 \times 10^8 \text{ K cm}^{-3}$, $\langle n_h \rangle = 0.05 \text{ cm}^{-3}$, and $B_{0y} = 3.0 \mu\text{G}$ at the $x = 0$ boundary plane. The parameters represent typical values in the diffuse ISM (P.C. Myers 1978; R. Beck 2001). This creates a primary shock wave whose normal vector is perpendicular to the mean magnetic field. The SNR is modelled as a young SNR (age = 750 years) with a late free-expansion phase. Here, our simulation is performed using the perpendicular shock of model 1 of T. Inoue et al. (2013) at $t = 700$ years (for more details see T. Inoue et al. (2013)).

Figure. 4.2 shows the Fourier power spectrum of velocity (red solid line) and magnetic field (blue dashed line). This spectrum is calculated using the turbulent regions. The velocity field shows the Kolmogorov spectrum $\propto k^{-5/3}$ with black solid line. Figure. 4.3 represents the two-dimensional slice of vorticity in post-shock region. Right contour shows the vorticity value. In post shock region, we see high vorticity due to the shock propagation.

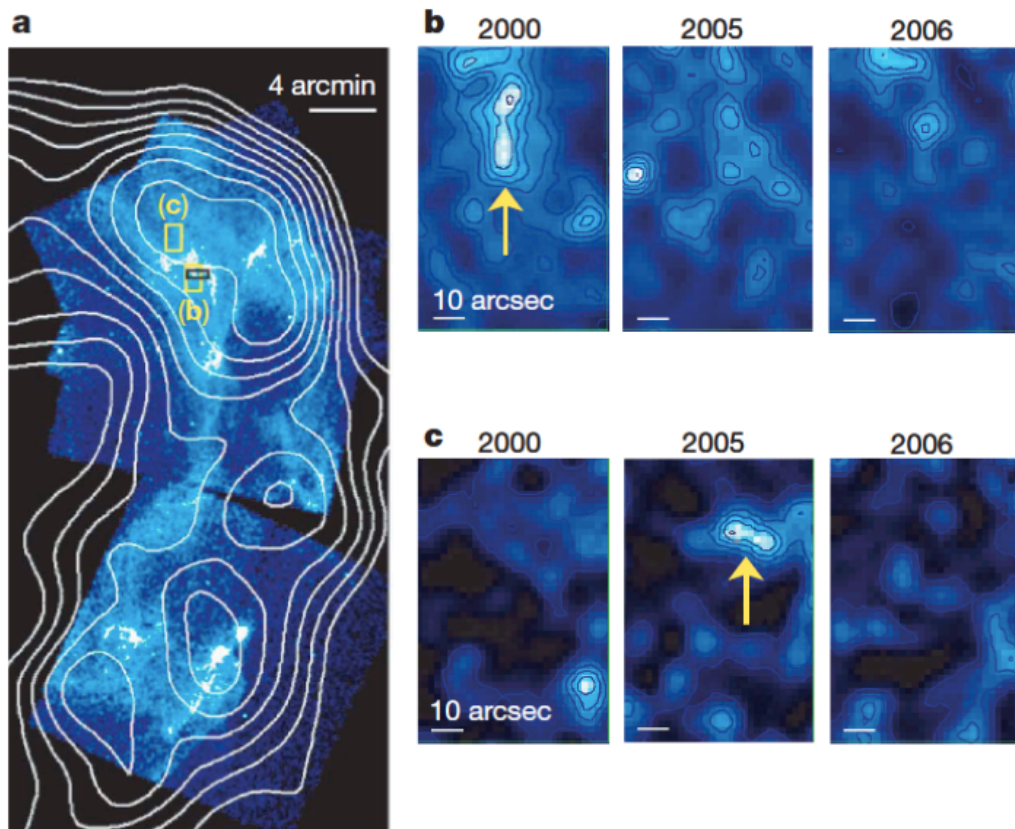


Figure 4.1: Observation : Chandra X-ray images of the western shell of SNR RX J1713.7-3946. Magnetic field amplification from μG to mG is interpreted by short time variability of synchrotron X-rays. See Y. Uchiyama et al. (2007) for a review.

From the data of Inoue et al. (2013)
One-phase medium

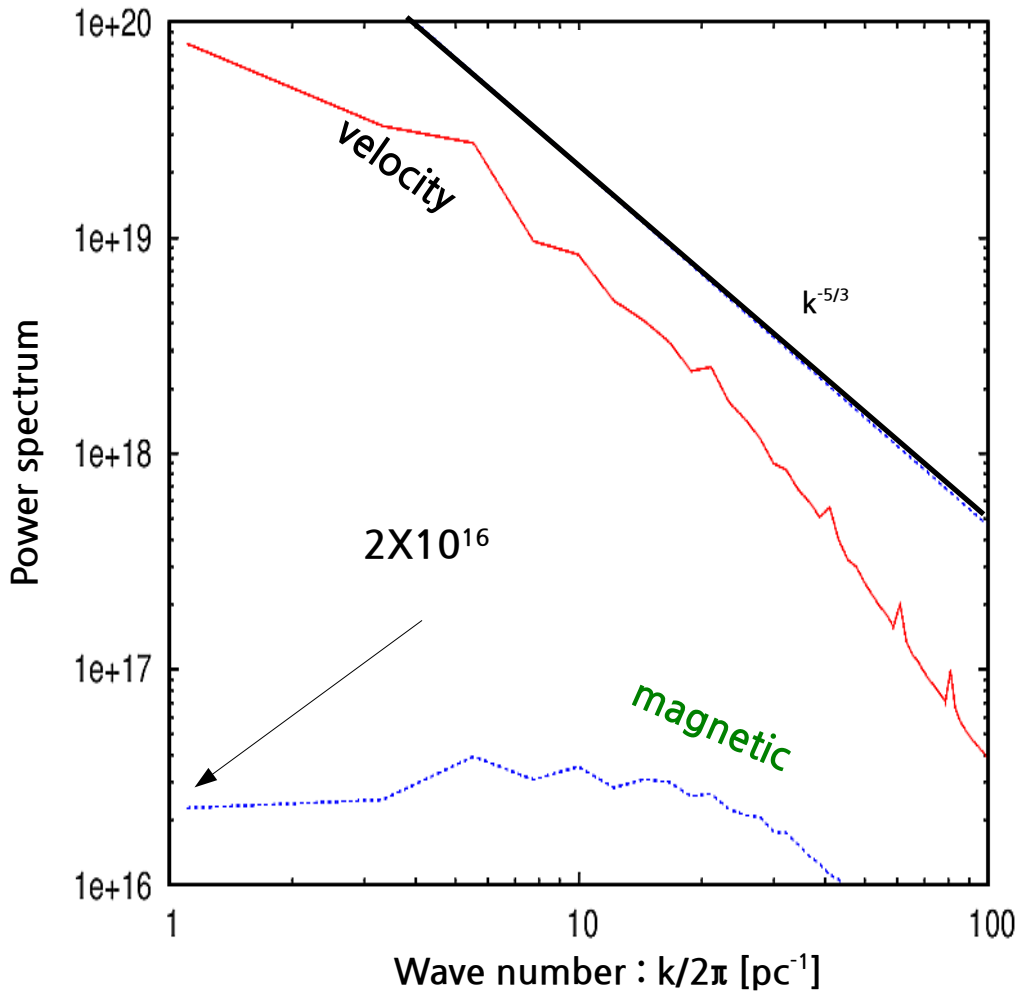


Figure 4.2: Fourier power spectrum of SNR turbulence in a one-phase medium (T. Inoue et al. (2013)). The black line represents the Kolmogorov law $k^{-5/3}$.

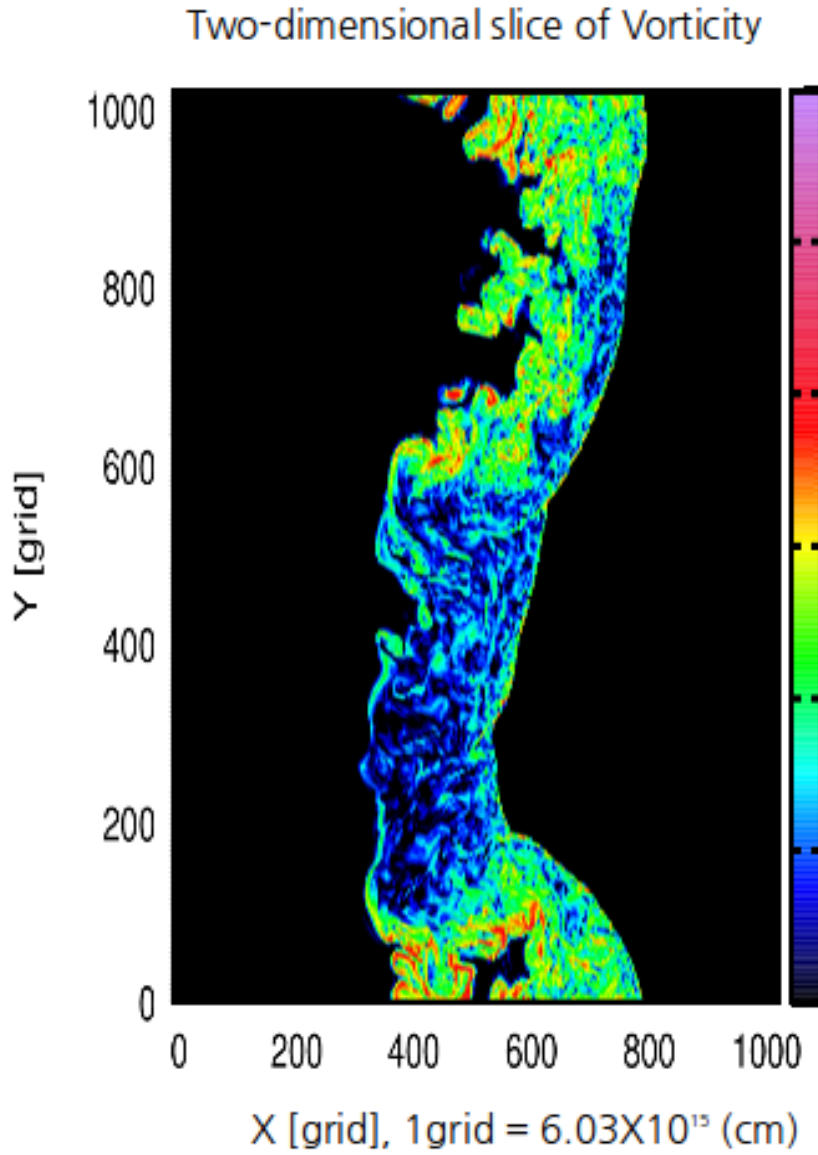


Figure 4.3: Contours in the xy-plane show the log scale of vorticity (cm^2/s). We selected the $Z = 201$ pc plane. Strong velocity shear is generated when dense and clumpy HI clouds are swept up by the shock.

2. Description of Multiphase Medium Simulation

T. Inoue et al. (2012) performed ideal three-dimensional magnetohydrodynamic (MHD) simulations of a strong shock wave ($v_{sh} \sim 2500$ km s⁻¹) propagating in a realistic multiphase ISM as the pre-shock region. We use the data for the perpendicular shock in T. Inoue et al. (2012) at $t = 750$ years as the background ISM to set up the electromagnetic field for our microscopic particle simulations. Here, we describe the simulation set-up.

To generate a multiphase ISM, they solved the ideal MHD equations including cooling, heating, and thermal conduction, which determine the unstable scale of thermal instability. They considered a net cooling function and photoelectric heating, and generated an inhomogeneous medium via thermal instability. The simulation considered ideal gas and used an adiabatic index of $\Gamma = 5/3$. The mean number density, initial thermal pressure, and initial magnetic field strength were taken to be $\langle n_0 \rangle = 2$ cm⁻³, $p/k_B = 2887$ K/cm³, and $B_{0y} = 5.0$ μ G, respectively, at the $x=0$ boundary plane. For the density, they imposed random density fluctuations with a thermally unstable state in the range 10 K $\leq T \leq 10^4$ K for effective cooling and heating. In the resulting clumpy cloud, they induced a high Mach number shock wave using a hot plasma with $p_h/k_B = 1 \times 10^9$ K/cm³ and $\langle n_h \rangle = 0.1$ cm⁻³. Figure. 4.4 shows the Fourier power spectrum of velocity (red solid line) and magnetic field (red dashed line). This spectrum is calculated using the turbulent regions of $x \in [1.0, 1.5] \cap y \in [1.3, 1.8] \cap z \in [0.0, 0.5]$. At large scales, $l = 2\pi/k > 0.03$ pc, the velocity field shows the Kolmogorov spectrum $\propto k^{-5/3}$ with black solid line.

A simulation box with size $L_{box} = 2$ pc is used, and the system resolution is $\Delta x = L_{box}/(\text{number of grid cells}) = 1.95 \times 10^{-3}$ pc,

where the number of uniform grid cells is 1024^3 . Periodic boundary conditions are used for the yz -plane. The above simulation resolution and boundary conditions are applied to both our one-phase and multiphase interstellar media.

Figure. 4.5 shows the number density distribution histogram for one-phase (upper) and multiphase interstellar medium (lower) at $t = 700$ years and 750 years, respectively. This histogram is calculated using the data of the small turbulent regions along the particle trajectories. For a multiphase interstellar medium case, it shows that the different from min to max is a factor of ~ 110 because, warm gas and cold cloud difference is a factor of 100.

Inoue et al. (2012)
Multiphase medium

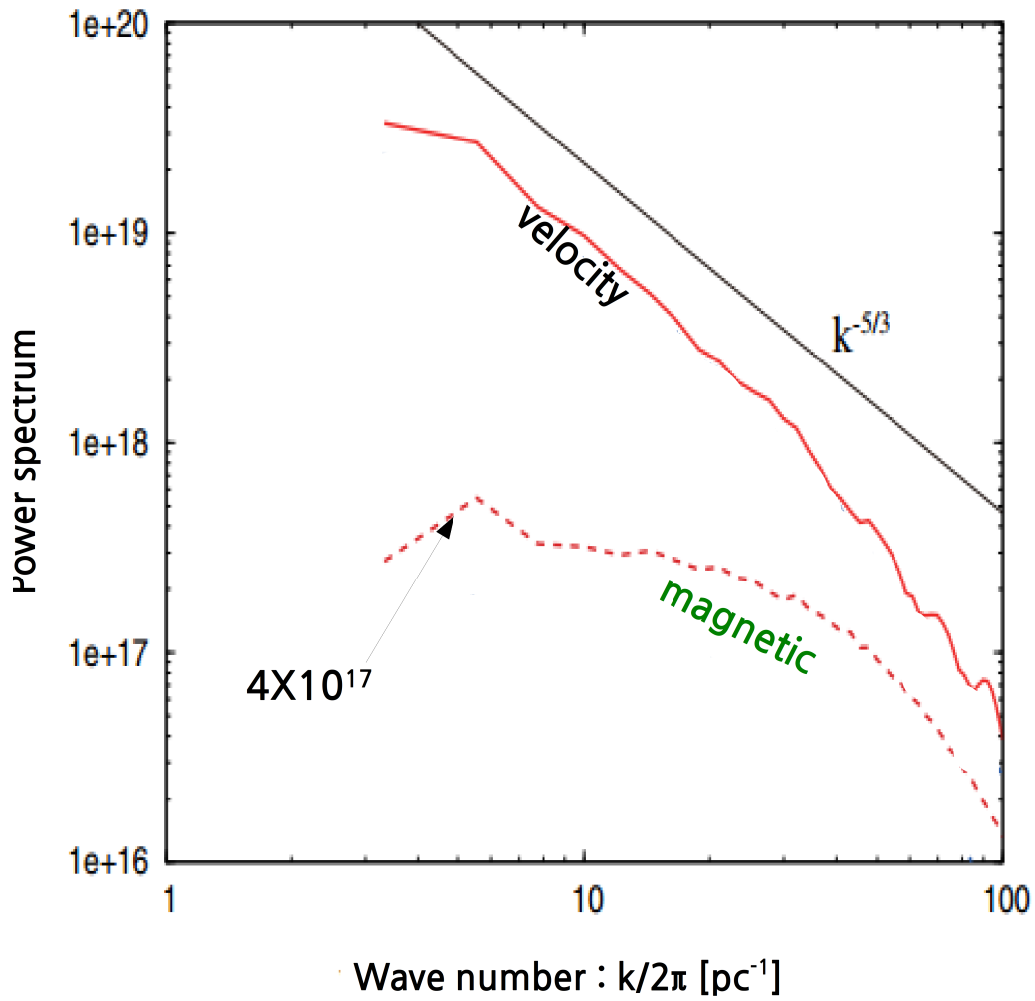


Figure 4.4: Fourier power spectrum of SNR turbulence in a multi-phase medium (T. Inoue et al. (2012)). The black line represents the Kolmogorov law $k^{-5/3}$. 56

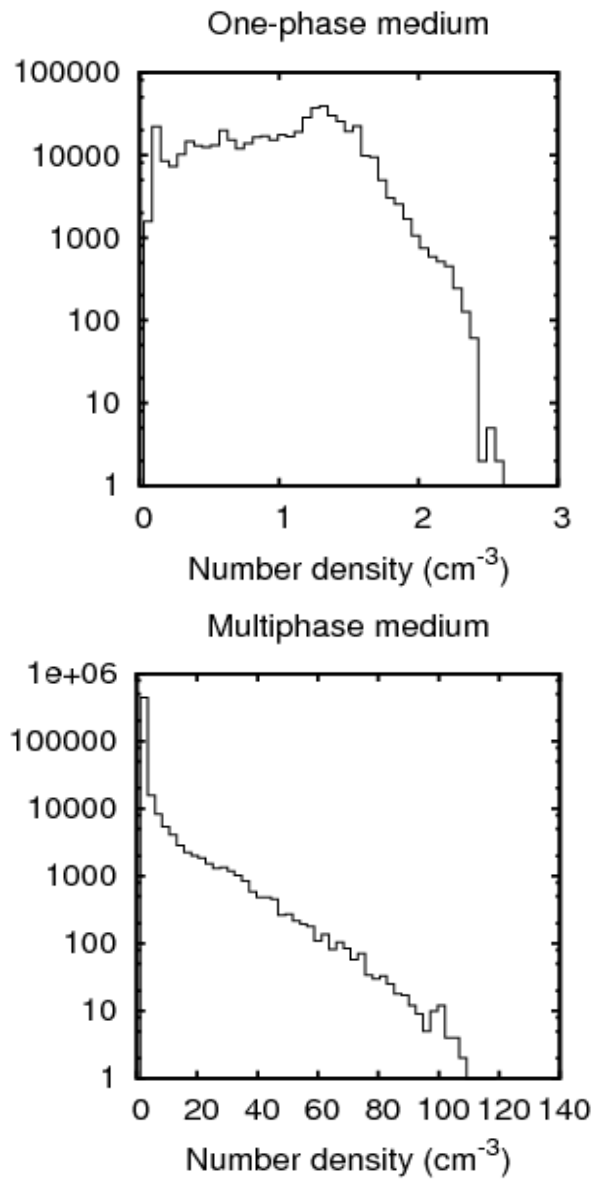


Figure 4.5: Density distribution. The upper figure shows the density of the one-phase medium. The lower figure shows the density of the multiphase medium. For the multiphase medium, the density range is larger than that of the one-phase medium by a factor of 110.

4.2 Description of Simulation Settings

4.2.1 Test Particle Simulations

The magnetized turbulent medium flows along the (positive) x -direction. We calculate the trajectories of CR particles using a snapshot of the MHD simulation data. We consider a collisionless environment for CRs because the mean free path, $\lambda = 1/n\sigma$, of relativistic particles is much larger than the gyroradius of CR particles. In the framework of non-relativistic ideal MHD, electromagnetic fields can be expressed as

$$\mathbf{E}(t, \mathbf{r}) = -\frac{\mathbf{V}(t, \mathbf{r})_{fluid} \times \mathbf{B}(t, \mathbf{r})}{c}, \quad (4.1)$$

where \mathbf{V} is the fluid velocity, \mathbf{B} is the local magnetic field at the position of the particles, and c is the speed of light. When we compute the Lorentz force acting on each CR particle, we interpolate \mathbf{V} and \mathbf{B} at the position of the particle before we calculate \mathbf{E} using Equation. 4.1. To trace the trajectories of CRs, we solve the relativistic equation of motion using a fourth-order Runge-Kutta method for updating particle information. The momentum of a particle is defined as

$$\mathbf{p} = \gamma m_i \mathbf{v}, \quad (4.2)$$

where \mathbf{v} is the velocity of a particle, γ is the particle Lorentz factor, and m_i is the mass of particle i . The equations governing the motion of relativistic charged particles are expressed as

$$\frac{d\mathbf{p}}{dt} = q_i(\mathbf{E} + \frac{\mathbf{v} \times \mathbf{B}}{c}), \quad (4.3)$$

$$\frac{d\mathbf{r}}{dt} = \frac{\mathbf{p}}{\gamma m_i}, \quad (4.4)$$

where q_i is the charge of particle i . The gyroradius, R_g , of particle i can be expressed by

$$R_g \approx \frac{\gamma m_i c^2}{|q_i| B} \quad \text{for } v \approx c. \quad (4.5)$$

The time discretization, Δt , for each particle is as follows:

$$t_r = \Omega_g^{-1} / N_d, \quad (4.6)$$

$$t_s = \frac{\Delta x}{N_d \cdot \max(|v_x|, |v_y|, |v_z|)}, \quad (4.7)$$

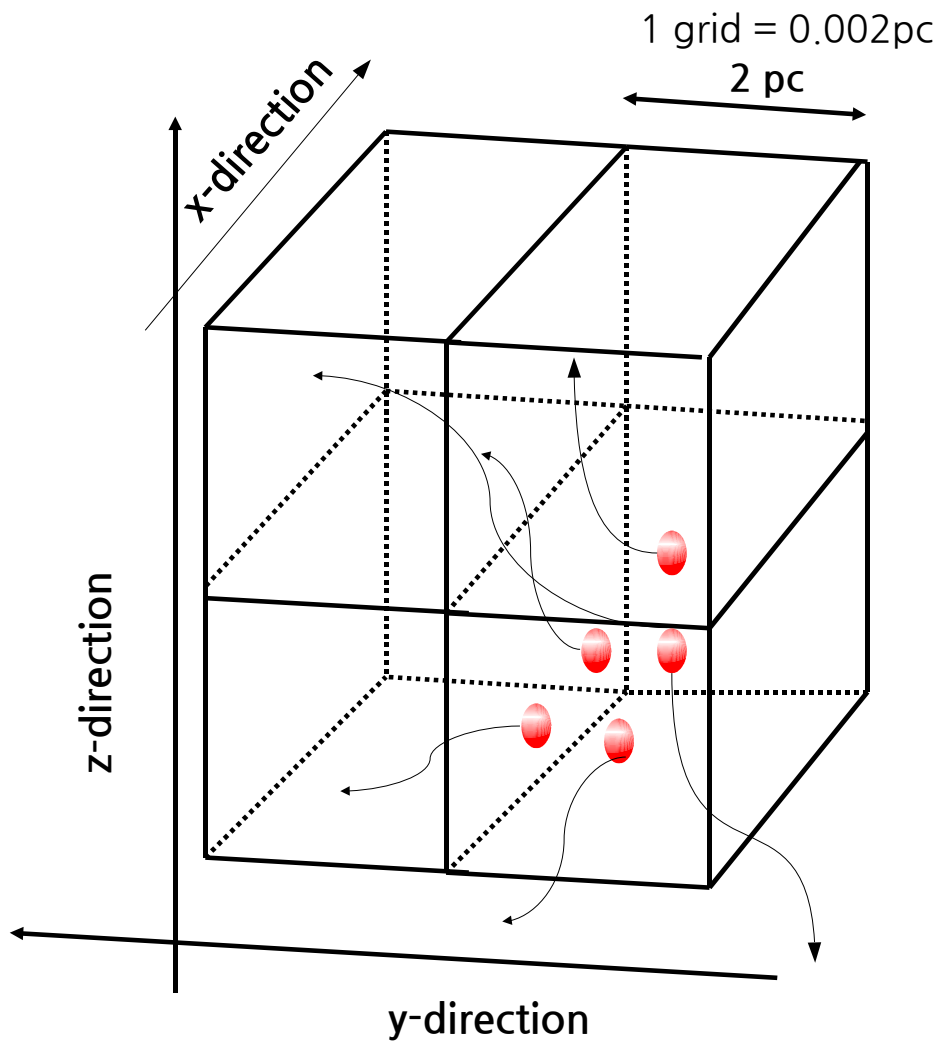
$$\Delta t = \min(t_r, t_s), \quad (4.8)$$

where $\Omega_g = |q_i|B/\gamma m_i c$ denotes the particle gyrofrequency and Δx is the size of a grid cell. N_d is the number of divisions, which determines the resolution of a particle trajectory. Because the time discretization is determined by the inverse of the gyrofrequency, as shown in Equation. 4.6., to trace the particle trajectory, Δt should be smaller than gyrofrequency. t_r is selected in our simulation when the particle energy is sufficiently small such that $R_g < \Delta x$, whereas t_s is selected for higher-energy cases satisfying $R_g > \Delta x$. For more details on R_g , see Section 4.3.2. We obtain Δt by considering Ω_g and the velocity components (v_x , v_y , and v_z) of a particle as well as using a sufficiently large value of N_d for tracing the trajectories of particles. For example, Δt was approximately 250 s for $\varepsilon_0 = 10^3$

TeV. In all calculations, we used $N_d = 10^3$, which is the value for keeping the errors of the Runge-kutta time-integration sufficiently small ($< 10^{-15}$ eV) for energy conservation.

4.2.2 Initial Settings

Figure. 4.6 shows a schematic picture of our simulation box using periodic boundary condition with yz -direction. Red circles and black arrows indicate the CR particles and their trajectories, respectively. Figure. 4.7 shows the initial position of particles in the post-shock region of multiphase medium case. We considered a box of size 0.3 pc, and distributed particle position information in the box. To keep the system statistically stable, 1000 particles were used in our simulation. Figure. 4.7 displays the velocities of particles in the box. We fixed the energy to know the dependence of energy with diffusion. The form of the velocity distribution is a delta function, and in velocity coordinates the distribution becomes a spatial distribution since velocities are randomly defined.



Periodic boundary condition for Y-Z direction.

Figure 4.6: Schematic figure of periodic boundary condition for test-particle calculation.

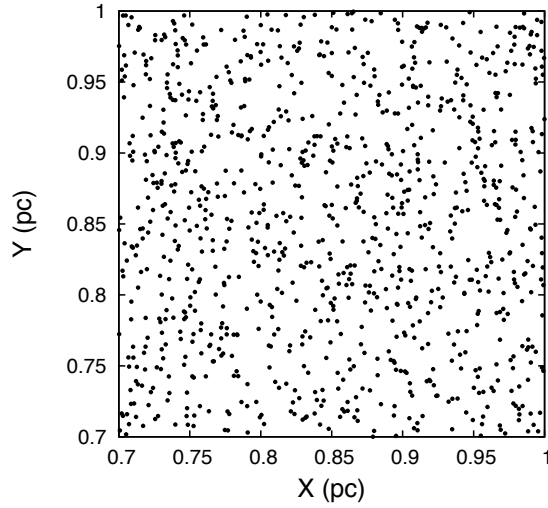


Figure 4.7: Initial particle positions. The particle distribution is random. The distribution range is $\min = 0.7$ pc, $\max = 1.0$ for x , y , and z , i.e., $(0.3 \text{ pc})^3$ (multiphase medium).

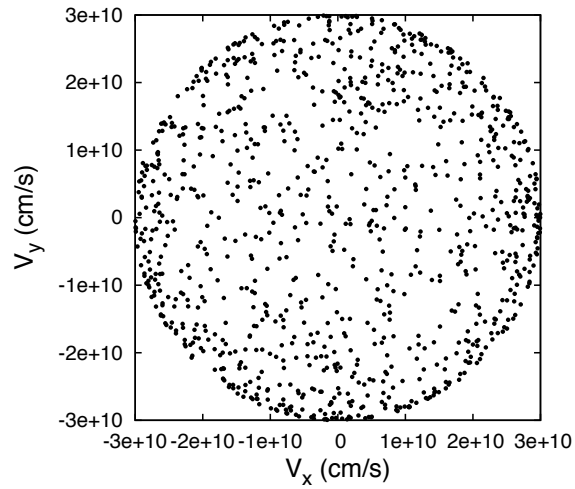


Figure 4.8: Initial particle velocities. This figure shows the $\varepsilon_0 = 10^{15}$ eV case. The particle directions are distributed by a random function (multiphase medium).

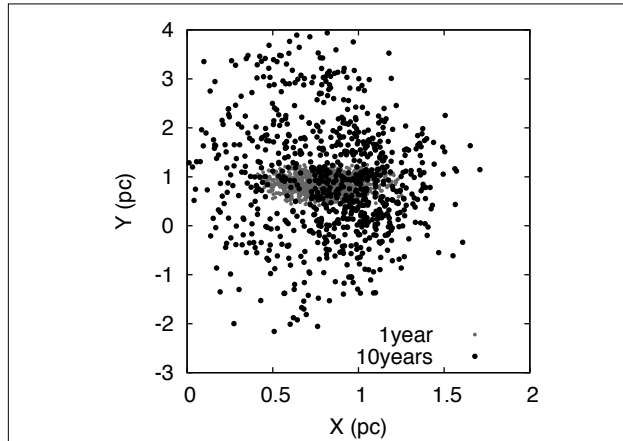


Figure 4.9: Particle distribution for $t = 1$ year and 100 years. This figure shows the xy plane. The particle positions at $t = 1$ year are shown in grey, and at $t = 100$ years they are represented by black dots. The particle positions represent escape from the post-shock region (multiphase medium).

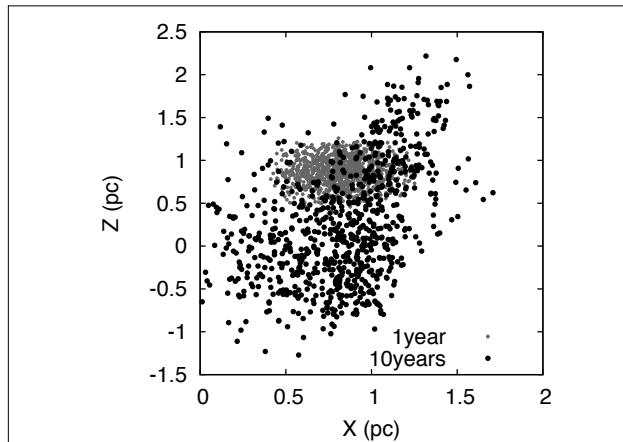


Figure 4.10: Particle distribution for $t = 1$ year and 100 years. This figure shows the xz plane. The particle positions at $t=1$ year are shown in grey, and at $t = 100$ years they are represented by black dots. The particle positions represent escape from the post-shock region (multiphase medium))

Figures. 4.8 and 4.10 show the transported particle distributions after 1 and 10 years of propagating. The initially particle distribution is random, however after 1 year the distribution shows anisotropy in the simulation. The basic setting for the fluid background velocity in T. Inoue et al. (2012) is moving in the negative z -direction. Thus particles motion tends to follow the velocity of fluid.

4.2.3 Runge-Kutta Method Error

To solve the relativistic equation of motion we use a fourth-order Runge-Kutta method. First, we performed a test calculation as follows:

$$\varepsilon = \gamma m_i c^2 \quad (4.9)$$

$$\mathbf{p} = \gamma m_i \mathbf{v} \quad (4.10)$$

$$\frac{d\mathbf{p}}{dt} = q_i \left(\mathbf{E} + \frac{\mathbf{v} \times \mathbf{B}}{c} \right) \quad (4.11)$$

where where ε is the energy of a particle and m is the mass of a particle. \mathbf{E} and \mathbf{B} are electric field and magnetic field, respectively and γ is the Lorentz factor including particle velocity \mathbf{v} . i denotes the kind of particle. Therefore, momentum has to be updated using the following steps:

$$\mathbf{p}_n \rightarrow \mathbf{p}_{n+1} \quad (4.12)$$

$$\varepsilon_{n+1} = p_{n+1}^2 c^2 + (m_i c^2)^2 \quad (4.13)$$

$$\gamma_{n+1} = \frac{\varepsilon_{n+1}}{m_i c^2} \quad (4.14)$$

$$\mathbf{v}_{n+1} = \frac{\mathbf{p}_{n+1}}{\gamma m_i} \quad (4.15)$$

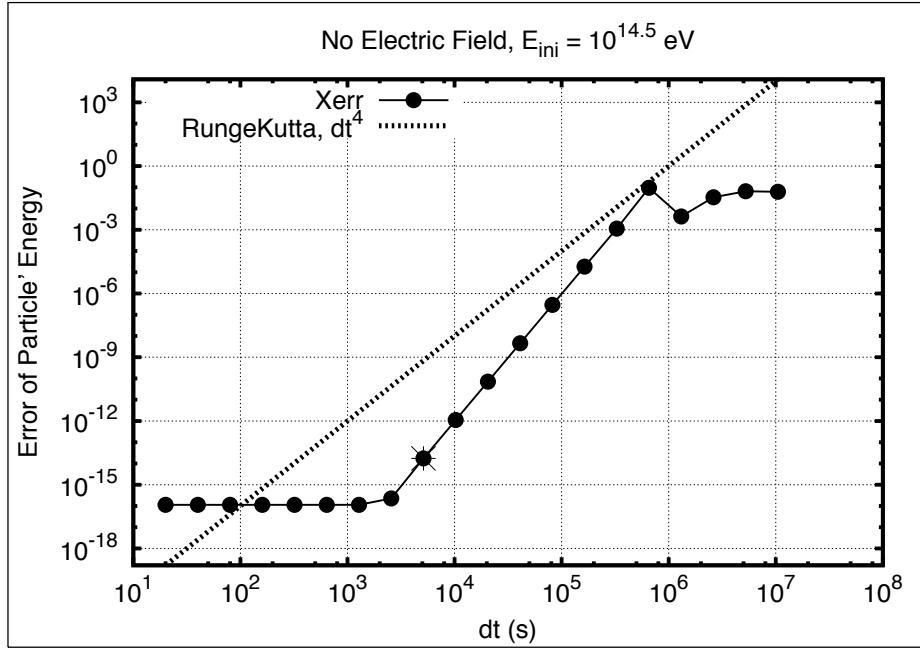


Figure 4.11: A fourth-order Runge-Kutta method error: the dotted line shows dt^4 , and the solid line with black circles is the error as a function of dt .

To check the accuracy of our simulation, we did not include the electric field due to energy conservation. We choose errors for the third calculation step. The Runge-Kutta error is approximately 10^{-15} for $dt < 100$ s with $\varepsilon_0 = 10^{14.5}$ eV (See Figures. 4.11 and 4.12). According to our test-calculation, our simulation follows a fourth-order Runge-Kutta method and the accuracy of the Runge-Kutta method is less than 10^{-15} eV.

Figure. 4.13 shows a test particle simulation using T. Terasawa et al. (2009). We confirmed that our test-particle simulation reproduces the results well.

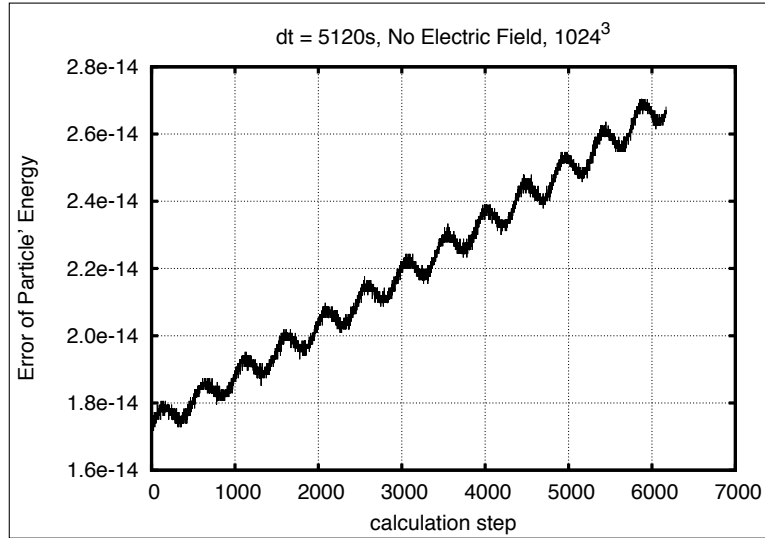


Figure 4.12: Energy increase as a function of calculation step (or time). dt is 5120 s, the gyrofrequency is $0.264^{-5}(s^{-1})$, and the calculation end time is 1 year.

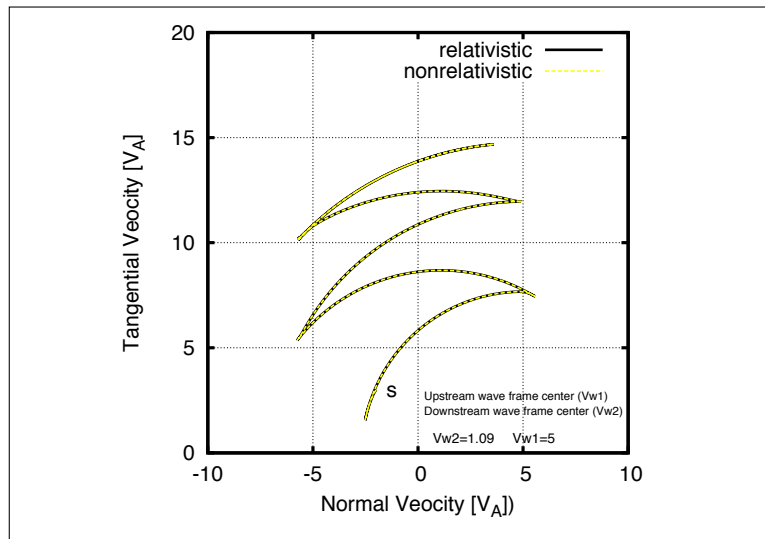


Figure 4.13: Confirmation the our test-simulation between non-relativistic and relativistic equations of motion by reproduction of T. Terasawa et al. (2009)

4.3 Diffusion Process in a One-Phase Medium

To calculate the transport of particles, we released sets of 10^3 protons with the same initial energies but isotropic velocity distributions in the computational frame. The range of the initial energies (ε_0) considered is 10^2 GeV to 10^3 TeV at intervals of $\log \varepsilon_0 = 0.5$. We assigned particle positions randomly in a cubic box region in the post-shock region (see region-I of Table 4.1). Initially the velocity directions are also random. To obtain the background fluid velocity and magnetic field we applied a linear interpolation to the MHD simulation data because the magnetic and fluid fields are defined at discrete points. We used periodic boundary conditions in the yz -direction as was done in the MHD simulation. We do not follow the time integration for orbits of particles that have escaped the x -boundary.

4.3.1 Diffusion in Configuration Space

To analyse the diffusion in configuration space we measure the displacement of transported particles. The displacement of a CR particle is expressed by

$$\Delta \mathbf{R}_j = \mathbf{R}_j(t) - \mathbf{R}_j(t_0), \quad (4.16)$$

where the notation j denotes the particle j and $R = \sqrt{\bar{x}^2 + \bar{y}^2 + \bar{z}^2}$, $\bar{x} = x_t - x_0$. The dispersion of displacement \mathbf{R} , hereafter $\sqrt{\langle (\Delta R)^2 \rangle}$, is expressed by

$$\sqrt{\langle (\Delta R)^2 \rangle} = \sqrt{\frac{\sum_{j=1}^{N_{ptls}} (\Delta \mathbf{R}_j)^2}{N_{ptls}}}, \quad (4.17)$$

where N_{ptls} denotes the total number of particles.

Here, we first show the transport properties of particles in our simulations as a function of $\log t$, and analyse the diffusion in configuration space. The values are averaged over $N_{ptls} = 10^3$ particles for each set of energies (ε_0). We calculated up to $t = 10^2$ years. To study the effect of changing the initial location, we defined several boxes for the initial CR particle locations. Table 4.1 shows the physical values of the background MHD data in the specific regions, defined as three-dimensional boxes. In this thesis, we mainly describe the particle distribution and background information of region-I as given in Table 4.1. This region is chosen to be in the dense, strong magnetic field post-shock region.

	region-I	region-II	post-shock region
$\langle \mathbf{B} \rangle$ (G)	1.262e-5	6.033e-6	1.102e-5
$\sqrt{\langle \delta \mathbf{B} \rangle^2}$ (G)	1.092e-5	9.306e-6	1.123e-5
$\langle \rho \rangle$ (cm^{-3})	1.303	1.2e-1	1.025
$\sqrt{\langle \delta \rho \rangle^2}$ (cm^{-3})	1.017	0.313	0.917

Table 4.1: Physical values in different simulation regions for one-phase medium. “region-I”, “region-II”, and “post-shock region” indicate the volume sizes occupied by the initial positions of particles in our simulation. region-I and region-II have volumes of $(0.3 \text{ pc})^3$ for the range 0.7 - 1 pc in xyz configuration space of our simulated data and $(0.2 \text{ pc})^3$ for 0.8 - 1.0 pc in x , 0.7 - 0.9 pc in y , and 1.0 - 1.2 pc in z configuration space of our simulated data. These regions are chosen to be in the dense, strong magnetic field post-shock region. Our simulation is performed in region-I for the one-phase medium.

Figure. 4.14 displays the travel distance (hear after displacement of R , $\sqrt{\langle (\Delta R)^2 \rangle}$, ($R = \sqrt{\bar{x}^2 + \bar{y}^2 + \bar{z}^2}$, $\bar{x} = x_0 - x_t$)) as a function

of log scale time. Used simulation region is a post-shock region in Table. 4.1. From the upper to lower black lines indicate the $\varepsilon_0 = 10^{13.5}$ eV to 10^{15} eV. Until $\log t = -0.5$ years, $\sqrt{\langle(\Delta R)^2\rangle}$ develops with linear function. It is expected due to $\mathbf{E} \times \mathbf{B}$ drift because, particles travel distance is still in a grid. Therefore, we consider time ranges from $\log t = -0.5$ to 2 years for high energy case. Figure. 4.15 shows the lower energy cases. Used simulation region is same as Figure. 4.14. In this study, we do not consider energies lower than $\varepsilon_0 = 10^{13}$ eV in our diffusion coefficient calculations.

The lines in Figure. 4.16 represent $\sqrt{\langle(\Delta R)^2\rangle}$ for protons with energies of $\varepsilon_0 = 10^{13.5}$ eV, 10^{14} eV, and $10^{14.5}$ eV, corresponding to R_g (gyroradius) $>$ Δx (grid size) (see Section 4.3.2 for more details). The uppermost dashed line in Figure. 4.16 shows the slope $t^{0.75}$. We can see the evolution of $\sqrt{\langle(\Delta R)^2\rangle}$ for $\varepsilon_0 = 10^{14}$, $10^{14.5}$ eV can be fitted by $t^{0.75}$, corresponding to fast diffusion or “superdiffusion”. Superdiffusion has been studied by A. Lazarian & H. Yan (2014) and S. Xu & H. Yan (2013). One of the reasons for superdiffusion is believed to be the wandering of magnetic field lines in a turbulent medium (see A.Lazarian & H. Yan (2014) for details).

$\sqrt{\langle(\Delta R)^2\rangle}$ for $\varepsilon_0 = 10^{13.5}$ eV shows ordinary diffusion, $t^{0.5}$ (black dotted line in Figure. 4.16), corresponding to a simple random walk. This random walk can be characterized by a diffusion coefficient, as we will discuss in the next section.

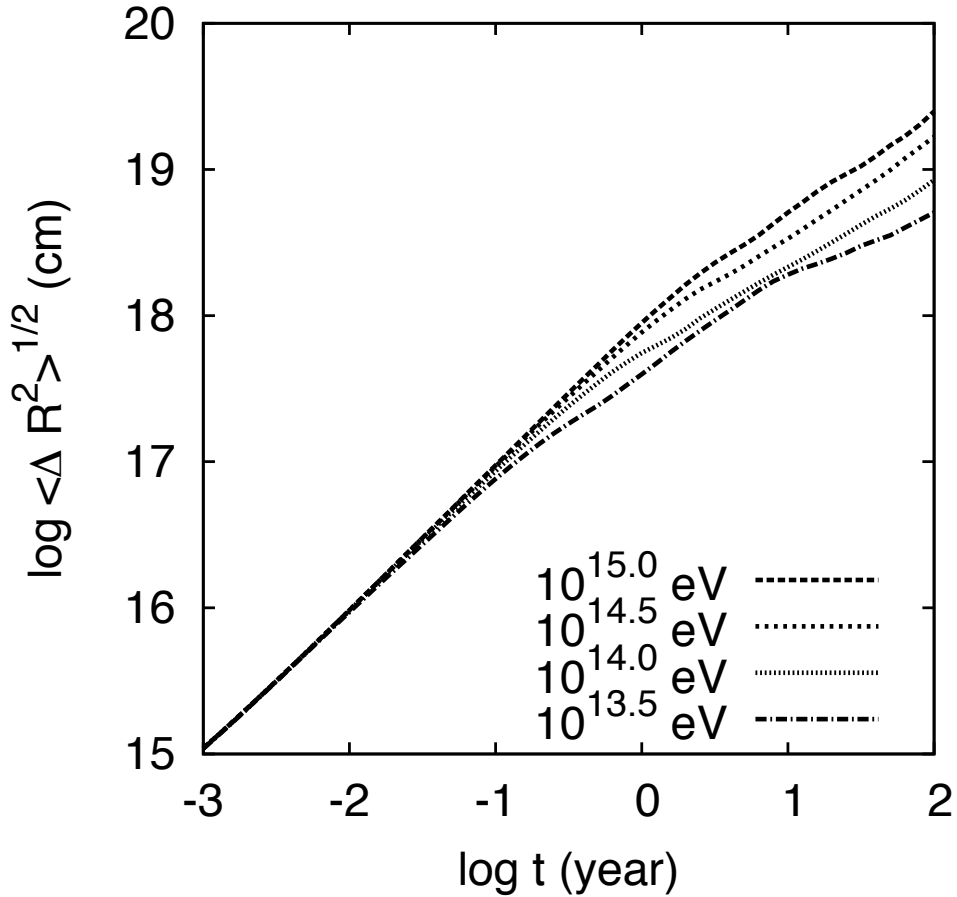


Figure 4.14: Travel distance of cosmic ray particles as a function of time. Black lines describe $\sqrt{\langle(\Delta R)^2\rangle}$ as a function of $\log t$. The initial energies of CRs, ε_0 , range from $10^{13.5}$ eV to 10^{15} eV, corresponding to R_g (gyroradius) $>$ Δx (grid size). In the $\varepsilon_0 = 10^{15}$ eV case, many particles escape from the post-shock region. Therefore, we only consider energies in the range $10^{13.5}$ eV to $10^{14.5}$ eV. In Figure. 4.16, we show a close-up of $\log t$ (year) larger than $\log t = -0.5$ (years).

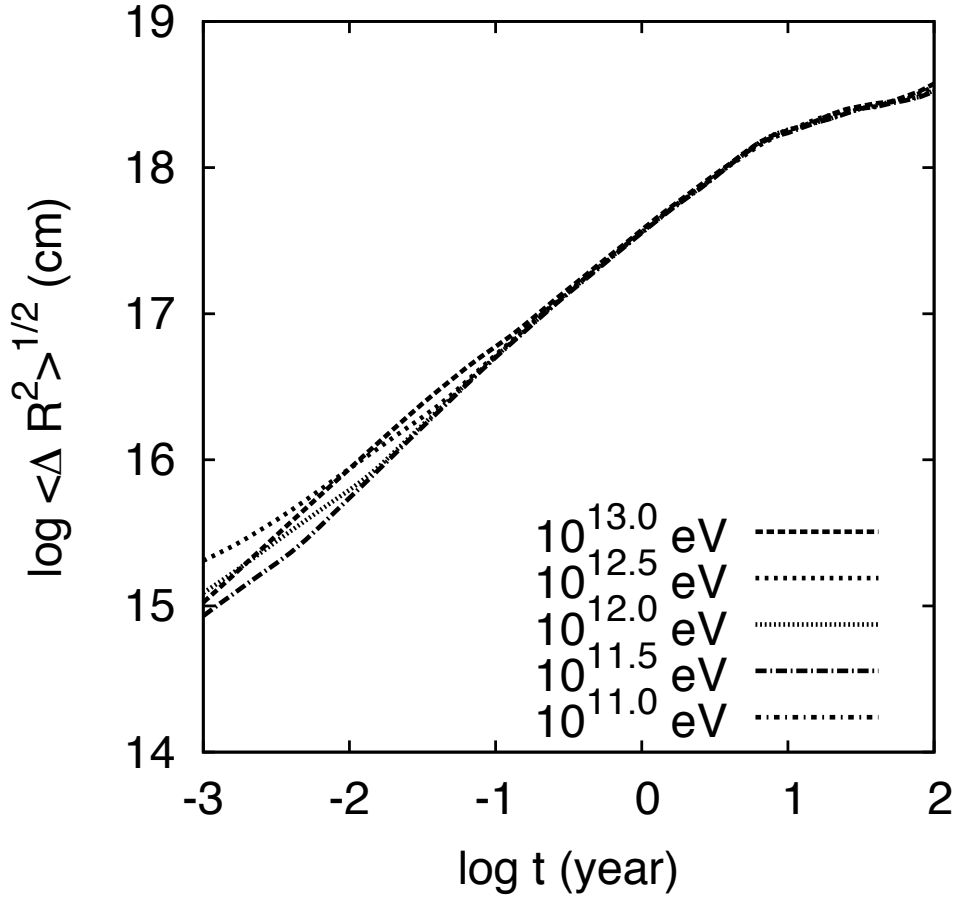


Figure 4.15: $\sqrt{\langle (\Delta R)^2 \rangle}$ ($R = \sqrt{\bar{x}^2 + \bar{y}^2 + \bar{z}^2}$, $\bar{x} = x_0 - x_t$) as a function of $\log t$. ε_0 ranges from 10^{11} eV to 10^{13} eV, corresponding to $Rg < \Delta x$. Therefore, most lines can be fit linearly due to simple motion along magnetic field lines, $\mathbf{E} \times \mathbf{B}$ drift.

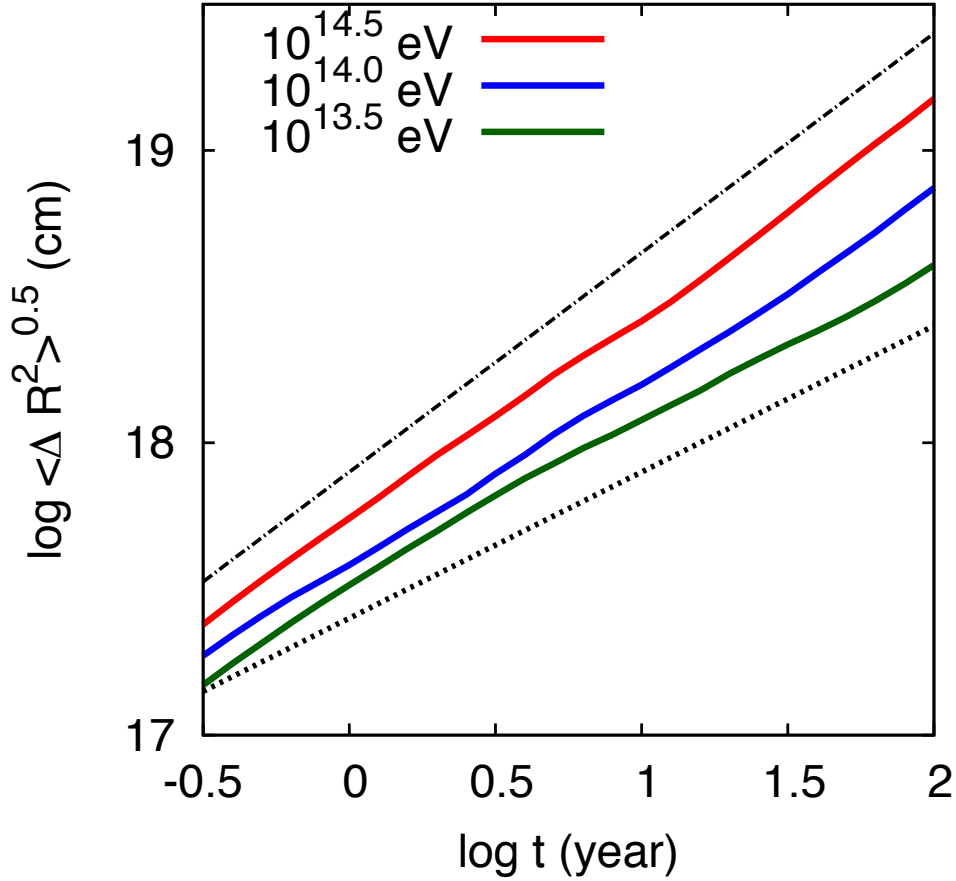


Figure 4.16: $\sqrt{\langle (\Delta R)^2 \rangle}$ ($R = \sqrt{\bar{x}^2 + \bar{y}^2 + \bar{z}^2}$, $\bar{x} = x_0 - x_t$) as a function of $\log t$. ϵ_0 ranges from $10^{13.5}$ eV to $10^{14.5}$ eV, corresponding to $Rg > \Delta x$. The values are averaged over 1000 particles for each set of energies. 100 years calculate. Red, blue and green lines indicate the curves of different energies. The red and blue lines are similar to the upper black dashed line that is proportional to $t^{0.75}$. And green line corresponds to black dot line which indicates slope = 0.5.

4.3.2 Comparison with Bohm Diffusion Rate

In this section, we quantify the diffusion coefficient of CR particles. According to the standard assumption of the theory of DSA, accelerated particles diffuse out in the plasma, in which the diffusive flux obeys Fick's law: the flux of particles is proportional to the gradient of flux density J.G. Kirt (2001). It is based on the assumption that charged particles are diffused isotropically by turbulent electromagnetic fields. In general, the diffusion coefficient can be expressed as

$$D(\mathbf{r}, \mathbf{p}) = \frac{1}{3} \lambda \mathbf{v}, \quad (4.18)$$

where λ and \mathbf{v} are defined as the mean scattering length and the particle velocity, respectively. The frequently used choice for the diffusion coefficient in DSA is that of "Bohm diffusion", expressed as

$$\lambda \approx R_g \left(\frac{B}{\delta B} \right)^2. \quad (4.19)$$

This depends on the degree of turbulence (A. Shalchi (2009); Hussein & Shalchi (2014)).

In our MHD simulation, however, the field strength shows the relation $\delta B \sim B$, as shown in Table 4.1. Therefore we use a simplified expression for Bohm diffusion with $\lambda \approx R_g$:

$$D_{Bohm}(\mathbf{r}, \mathbf{p}) = \frac{1}{3} R_g \mathbf{v} \sim \frac{1}{3} R_g c. \quad (4.20)$$

This model, $D_{Bohm}(\mathbf{r}, \mathbf{p})$, has been used by many authors (e.g., F. Skilling (1975)).

In order to quantify the diffusion of CR particles in our background field, we define $D_{sim}(t)$ as

$$D_{sim}(t) = \frac{\langle(\Delta R)^2\rangle}{6t}. \quad (4.21)$$

We compare this quantity to the Bohm diffusion coefficient. If $\langle(\Delta R)^2\rangle$ is proportional to t , $D_{sim}(t)$ is constant in time and can be used as the diffusion coefficient in the standard diffusion equation for CR particles. Strictly speaking, $D_{sim}(t)$ is not the diffusion coefficient if it is not constant in time, such as for superdiffusion. Even in that case, however, $D_{sim}(t)$ is a measure of the diffusion of CR particles.

Figure. 4.17 shows the relation between gyroradius and the ratio of D_{sim}/D_{Bohm} , calculated with Equations. 4.20 and 4.21, for different values of ε_0 . Both diffusion coefficients, D_{sim} and D_{Bohm} , are summarized in Table 4.2. The values are calculated for 10^3 particles at five different values of ε_0 at intervals of $\log \varepsilon_0 = 0.5$. The left panel of Figure. 4.17 shows the gyroradius in units of pc, and the right panel shows the ratio between D_{sim} and D_{Bohm} . Each symbol along the dashed lines corresponds to the gyroradius at a different time. Filled and open circles correspond to $t = 10^2$ years and 10 years, respectively. Note that the smallest (L_{min}) and largest (L_{max}) turbulent scales in our simulation correspond to a few grids and a few hundreds grids, respectively (T. Inoue et al. 2013). The grid size corresponds to $\Delta x = 6.03 \times 10^{15}$ cm. Particles are supposed to be reflected by the turbulent field when $L_{min} < R_g < L_{max}$. For the case of $R_g < L_{min}$, particles only see an almost uniform field, and thus are expected to experience $\mathbf{E} \times \mathbf{B}$ drift. In this case the travel distance is proportional to t at early times. In Figure. 4.17,

particles with $\varepsilon_0 = 10^{14}$ eV and $10^{14.5}$ eV satisfy $L_{min} < R_g < L_{max}$. For these particles, the diffusion can be expressed by superdiffusion (S. Xu & H. Yan 2013), see Figure. 4.16. Even for these cases, however, the differences between D_{sim} and D_{Bohm} are not so large. The value of D_{sim}/D_{Bohm} decreases with increasing ε_0 and remains of order unity. Thus, the Bohm diffusion coefficient description for CR diffusion can be justified by our test particle simulations, at least for shocked SNRs. We discuss this further in Section 4.3.4.

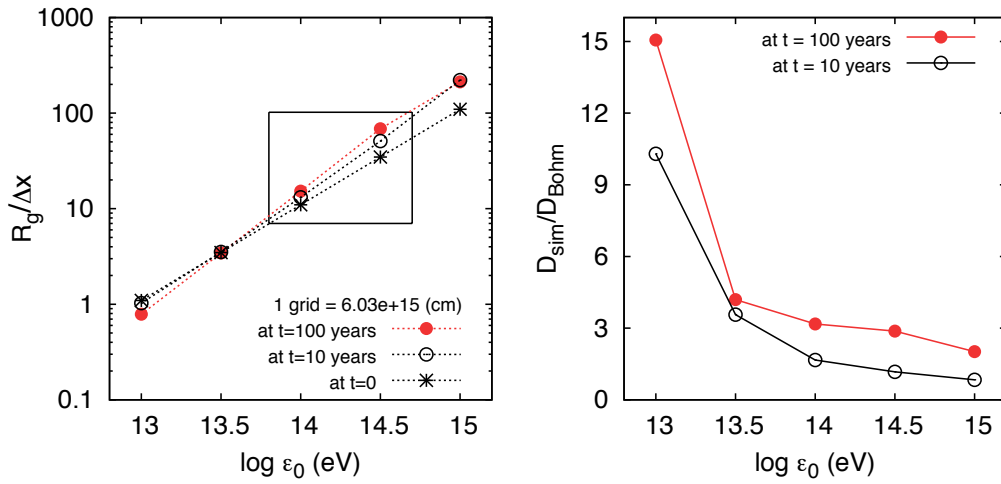


Figure 4.17: Gyroradius and diffusion coefficient as a function of cosmic ray energy. The left panel is gyroradius in units of pc, shown by dashed lines. The right panel is the ratio between the estimated values (D_{Bohm}) and the simulation values (D_{sim}) from Equations. 4.20 and 4.21, shown as a function of $\log \varepsilon_0$ by solid lines. The results at 10 years and 10^2 years are shown by open black circles and filled black circles, respectively. Stars show the case $t = 0$.

	t = 10 years		t = 100 years	
log ε_0 (eV)	D_{sim} (cm ² /s)	D_{Bohm} (cm ² /s)	D_{sim} (cm ² /s)	D_{Bohm} (cm ² /s)
15.0	1.120e+28	1.334e+28	2.575e+28	1.277e+28
14.5	3.593e+27	3.073e+27	1.189e+28	4.134e+27
14.0	1.318e+27	7.920e+26	2.916e+27	9.189e+26
13.5	7.578e+26	2.126e+26	8.687e+26	2.071e+26
13.0	6.374e+26	6.191e+25	7.136e+26	4.740e+25

Table 4.2: Difference between D_{sim} and D_{Bohm} as a function of ε_0 .

4.3.3 Superdiffusion

Superdiffusion has been reported in simulations by A. Lazarian & H. Yan (2014) and S. Xu & H. Yan (2013). We compare our results with S. Xu & H. Yan (2013) to investigate the existence of superdiffusion in our simulations. The pre-shock magnetic field lines in our simulations are laminar and not turbulent, and the turbulence is created by the RMI (T. Inoue et al. 2013) driven by the propagation of a blast wave. In contrast, S. Xu & H. Yan (2013) drove turbulence by solenoidal forcing in Fourier space. Note that both our simulations and those of S. Xu & H. Yan (2013) follow the Kolmogorov scaling law of turbulence expressed by $\varepsilon(k) \propto k^{-\frac{5}{3}}$.

We calculated the dispersion $\langle(\Delta\xi_{\perp})^2\rangle^{1/2}$ as a function of $\langle|\Delta\xi_{\parallel}|\rangle$ for up to 10^2 years, the results of which are shown in Figures. 4.18 and 4.19, where ξ_{\perp} is perpendicular to the mean magnetic field (B_{0y}), and ξ_{\parallel} is the displacement along the mean magnetic field. Figure 4.18 shows the dispersion $\langle(\Delta\xi_{\perp})^2\rangle^{1/2}$ as a function of $\log t$. Used ε_0 ranges from 10^{12} eV to 10^{15} eV and considered time scale corresponds to Figure. 4.14. Figure 4.19 represents a close-up of $\log t$ larger than $\log t = -0.5$ years and used data region is region-I of Table 4.1.

The upper and lower black dashed lines of Figure. 4.19 represent $\langle(\Delta\xi_{\perp})^2\rangle^{1/2} \propto t^{0.75}$, respectively. The slope close to 1.5 might be a manifestation of wandering magnetic field lines analogous to Richardson diffusion, as discussed in A. Lazarian & H. Yan 2013. This might be the reason for the superdiffusion found in Figure. 4.16. However, the higher-energy particles do not show the 1.5 slope of Figure. 4.19, because the gyroradius of higher-energy particles is larger than the injection scale of turbulence. The particles with smaller energies show an almost linear slope, which corresponds to simple diffusion as shown in Figure. 4.16.

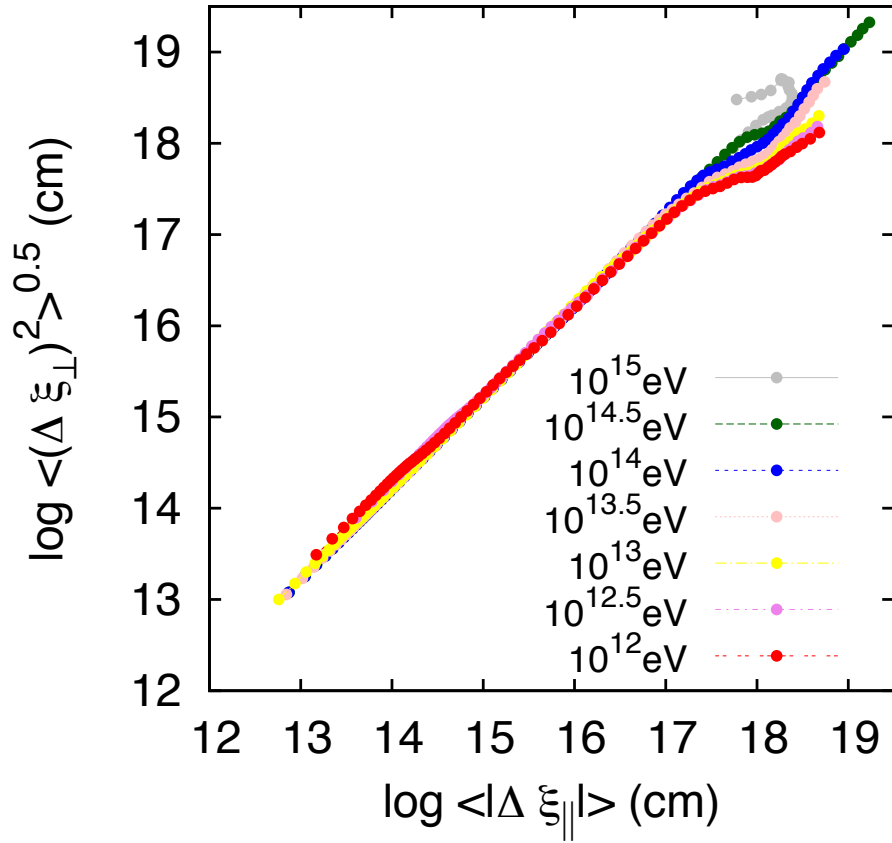


Figure 4.18: Relation between travel distances in the directions parallel and perpendicular to the mean magnetic field lines. This figure shows $\langle (\Delta \xi_{\perp})^2 \rangle^{1/2}$ as a function of $\langle |\Delta \xi_{\parallel}| \rangle$ including at early times.

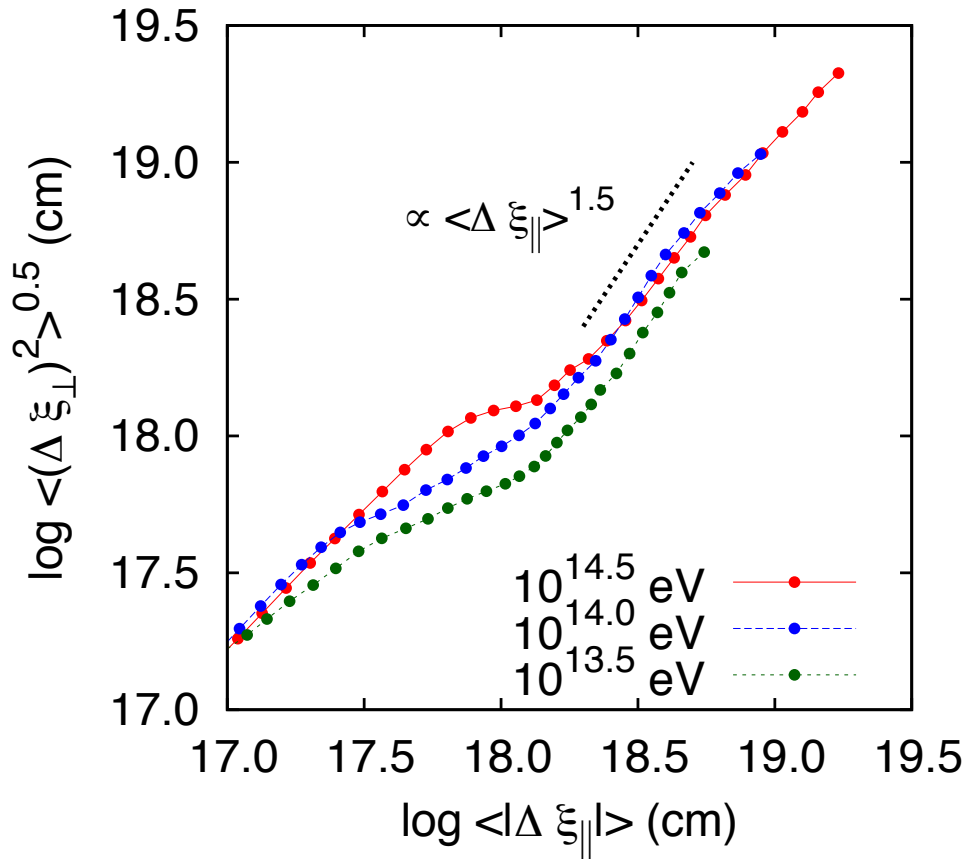


Figure 4.19: Relation between travel distances in the directions parallel and perpendicular to the mean magnetic field lines. This figure shows $\langle (\Delta \xi_{\perp})^2 \rangle^{1/2}$ as a function of $\langle |\Delta \xi_{\parallel}| \rangle$. In Figure. 4.18, we show a close-up of $\log \langle |\Delta \xi_{\parallel}| \rangle > 17$ cm.

4.3.4 Richardson Diffusion

To explain superdiffusion, A. Lazarian & H. Yan (2014) suggested Richardson diffusion that is explained as the divergence (wandering) of magnetic field lines. To explain Richardson diffusion, we follow the description of A. Lazarian & H. Yan (2014), see Figure. 1. of their paper. For the Kolmogorov turbulence case, the cascade rate is defined as:

$$\epsilon \approx v_l^3/l = \text{const.} \quad (4.22)$$

The relative velocities of particles increase as the scale of motions increases according to the 1/3 law. This is described by

$$v(l) \sim v_0(l/L)^{1/3}, \quad (4.23)$$

where v_l is the difference of the velocities of particles separated by distance l , v_0 is the injection velocity at scale L . Using $v_l \sim (d/dt)l(t)$, we can obtain the follow equation:

$$\frac{d}{dt}l(t) \sim (\epsilon l)^{1/3}. \quad (4.24)$$

From the above equations, we obtain the solution as

$$l^2 \sim \epsilon t^3. \quad (4.25)$$

4.3.5 Diffusion in Energy Space

In a turbulent medium, second order Fermi acceleration is expected in which some particles gain energy stochastically for a sufficiently long time interval. This can be considered to be a random walk in energy space ($\Delta\varepsilon \propto \sqrt{t}$).

We calculated for up to 10^2 years for 10^2 TeV and 10^3 TeV protons. Figure. 4.20 shows the magnitude of the particle energy, $\Delta\varepsilon$, as a function of $\log t$. The dashed lines in both panels represent energy gain proportional to $t^{0.5}$. This demonstrates the stochastic behaviour of energy gain in our simulation. However, the energy gain rate is very small within 10^2 years, less than 1% of the original energy.

4.3.6 Effect of Electric Field

As we mentioned in Section 4.2.1, the electric field in the comoving frame of the ISM vanishes in the ideal MHD limit. The strength of the electric field in the computational frame is smaller than the magnetic field strength by a factor of v/c (see Equation. 4.1). Therefore, the force due to the electric field is small in comparison to the force due to magnetic field. In this section, we study the effect of electric field on the diffusion of CRs in the ISM. Figure. 4.21 shows the results of diffusion calculations with and without a background plasma (\mathbf{E}). It shows that the inclusion of \mathbf{E} results in slightly larger diffusion but the difference is rather limited ($< 34\%$). Therefore, electric fields are less important for studying diffusion in configuration space, but they are critical to studying the diffusion in energy space.

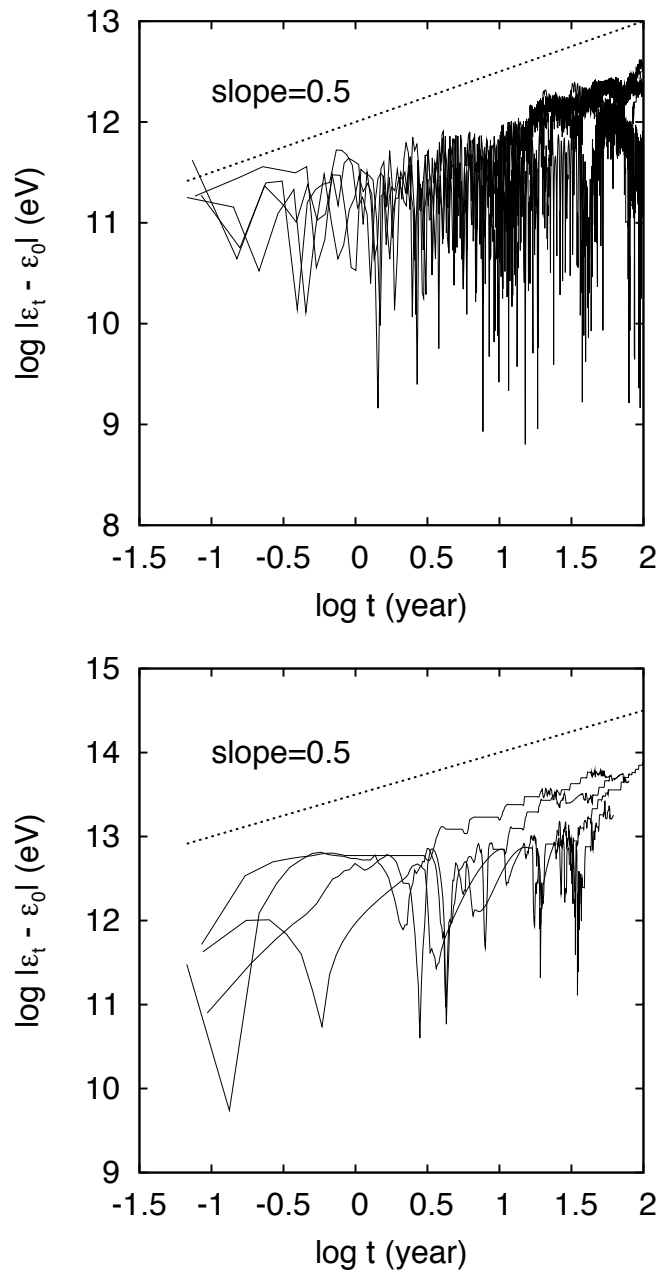


Figure 4.20: Magnitude of the change in particle energy $\Delta\varepsilon$ as a function of t for protons with initial energies of $\varepsilon_0 = 10^{14}$ eV and $\varepsilon_0 = 10^{15}$ eV.

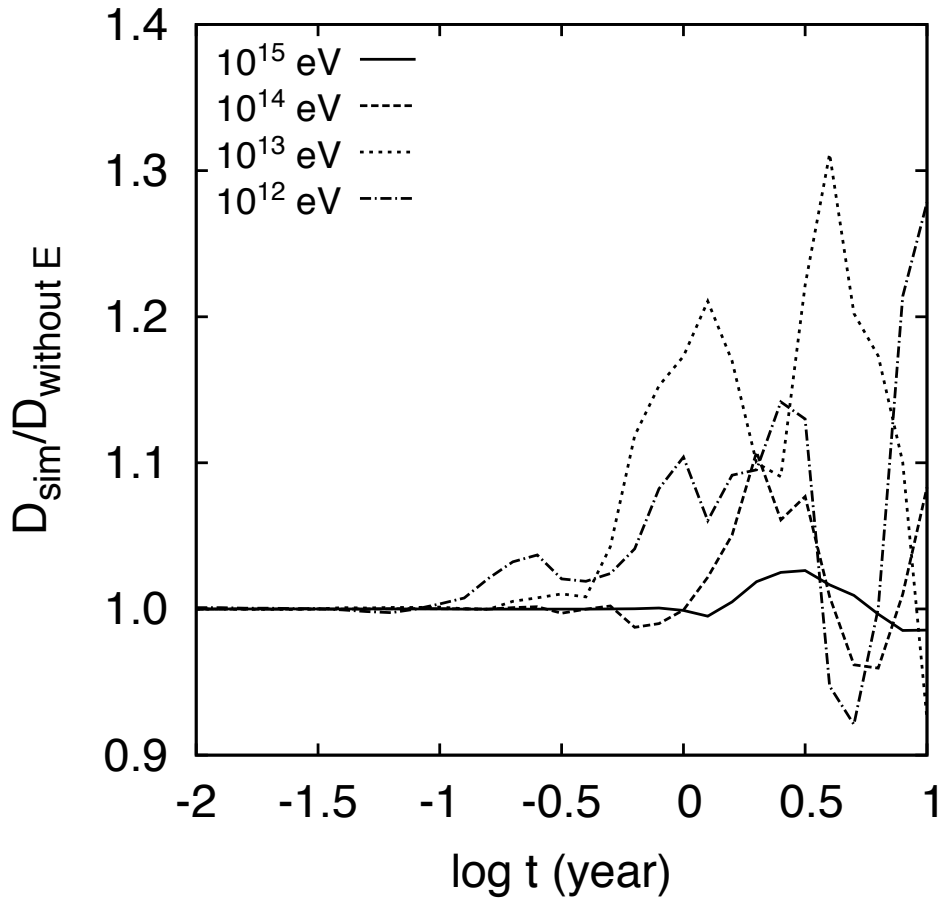


Figure 4.21: Comparison between diffusion coefficient ratios for results with \mathbf{E} and without \mathbf{E} for the energy range 1 TeV to 10^3 TeV.

4.4 Diffusion Process in a Multiphase Medium

4.4.1 Diffusion in Configuration Space

The main calculation and conditions for a multiphase medium are the same as described for the one-phase medium of Section 4.3. In this section, we describe the diffusion process using a multiphase medium. Therefore, we omit the calculation method because it is the same as the description in Section 4.3.

	region-I	post-shock region
$\langle \mathbf{B} \rangle$ (G)	2.36e-5	2.13e-5
$\sqrt{\langle \delta \mathbf{B} \rangle^2}$ (G)	3.36e-5	3.53e-5
$\langle \rho \rangle$ (cm ⁻³)	2.15	5.65
$\sqrt{\langle \delta \rho \rangle^2}$ (cm ⁻³)	1.84	5.22

Table 4.3: Physical values in different simulation regions for the multiphase medium. “region-I” and “post-shock region” indicate the volume sizes occupied by the initial positions of particles in our simulation. region-I and post-shock region have volumes $(0.3 \text{ pc})^3$ for the range 1.5 - 1.8 pc in xyz configuration space and $(2 \text{ pc})^3$ in 1.6 - 1.8 pc of x , 0.7 - 0.9 pc of y , and 1.4 - 1.6 pc of z configuration space. Our simulation is started in region-I for the multiphase medium.

Here, we show the transport properties of particles in our simulations as a function of $\log t$, and analyze the diffusion in configuration space. The lines in Figure. 4.22 represent the value of $\sqrt{\langle (\Delta R)^2 \rangle}$ for protons with energies of $\varepsilon_0 = 10^{13.5} \text{ eV}$, 10^{14} eV , and $10^{14.5} \text{ eV}$, corresponding to R_g (gyroradius) $> L$ (injection scale) (see Section 4.3.2 for more details). The values are averaged over $N_{ptls} = 10^3$ particles for each set of energies (ε_0). The calculation is run for a sufficiently

long time, up to $t = 10^2$ years from the time of the snapshot for young SNRs of age ~ 700 years.

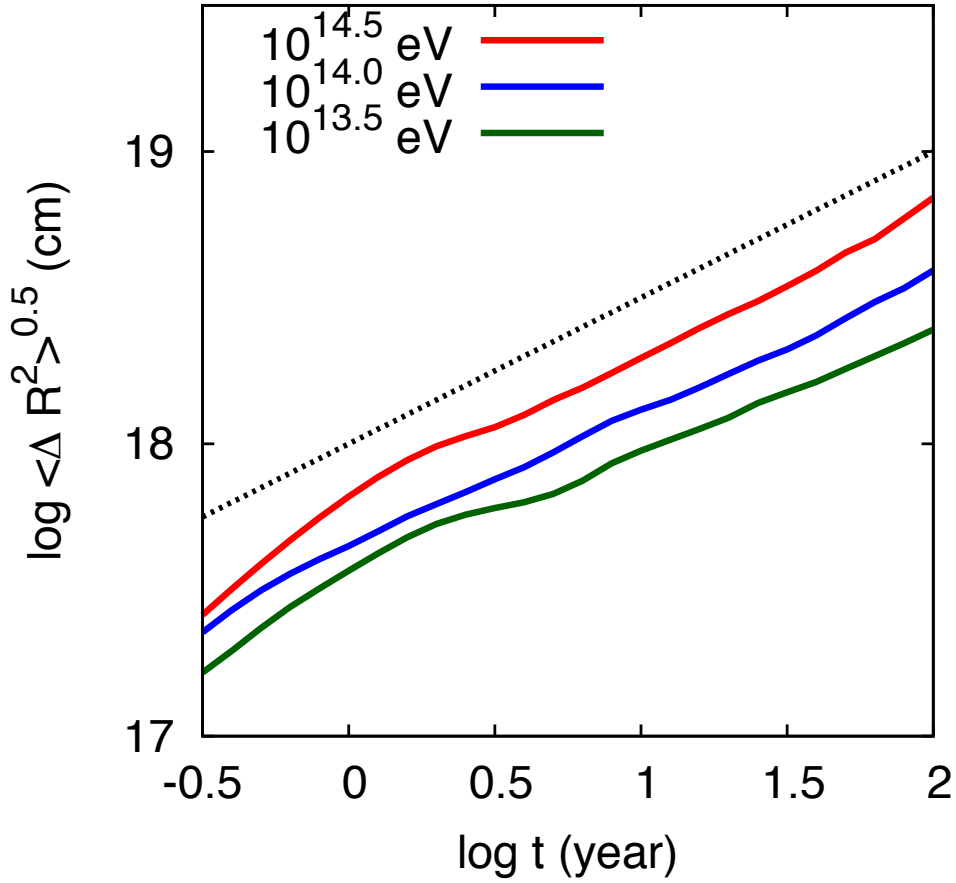


Figure 4.22: $\sqrt{\langle (\Delta R)^2 \rangle}$ ($R = \sqrt{\bar{x}^2 + \bar{y}^2 + \bar{z}^2}$, $\bar{x} = x_0 - x_t$) as a function of $\log t$. ε_0 ranges from $10^{13.5}$ eV to $10^{14.5}$ eV, corresponding to $Rg > \Delta x$.

In the cases shown, the evolution of $\sqrt{\langle(\Delta R)^2\rangle}$ is described by standard diffusion (or slowest diffusion), the so-called Bohm diffusion, that is proportional to $t^{0.5}$ for all energies, $\varepsilon_0 = 10^{13.5}$ eV, $\varepsilon_0 = 10^{14}$ eV, and $\varepsilon_0 = 10^{14.5}$. The black dotted line in Figure. 4.22 is the slope $t^{0.5}$ at both energies, corresponding to random walk.

4.4.2 Comparison with Bohm Diffusion Rate

log ε_0 (eV)	t = 10 years		t = 100 years	
	D_{sim} (cm ² /s)	D_{Bohm} (cm ² /s)	D_{sim} (cm ² /s)	D_{Bohm} (cm ² /s)
15.0	5.839e+27	8.000e+27	7.520e+27	6.584e+27
14.5	2.044e+27	2.497e+27	2.560e+27	2.163e+27
14.0	9.054e+26	7.906e+26	8.116e+26	6.437e+26
13.5	4.745e+26	3.193e+26	3.193e+26	2.038e+26
13.0	3.314e+26	2.015e+26	2.015e+26	6.225e+25

Table 4.4: Differences between D_{sim} vs. D_{Bohm} as a function of ε_0 . We used the region-I volume results shown in Table 4.3.

Figures. 4.23 and 4.24 show the relation between gyroradius and the ratio of D_{sim}/D_{Bohm} for different ε_0 s, calculated using Equations. 4.20 and 4.21. The values are calculated for 10^3 particles at nine different given values of ε_0 at intervals of $\log \varepsilon_0 = 0.5$. Figure. 4.23 shows the gyroradius in units of pc. The symbols along the dashed lines corresponds to the gyroradius at different times. Figure. 4.24 represents the difference between D_{sim} and D_{Bohm} , where the black and red solid lines correspond to $t = 10$ years and $t = 10^2$ years, respectively.

Applying the Bohm diffusion process, the differences in D_{sim}/D_{Bohm} are less than a factor of 1 at both times in Figure. 4.24, and decrease

with increasing ε_0 . This can be interpreted as follows: the differences in D_{sim}/D_{Bohm} are significantly small. Thus, our result precisely justifies the observational result that considered Bohm diffusion, Y. Uchiyama et al. (2007). The diffusion coefficients are summarized in Table 4.4.

We calculated the dispersion $\sqrt{\langle(\Delta\xi_{\perp})^2\rangle}$ as a function of $\langle|\Delta\xi_{\parallel}|\rangle$ for up to 10^2 years, the result of which is shown in Figure. 4.25. ξ_{\perp} is perpendicular to the mean magnetic field (B_{0y} ; perpendicular shock), and ξ_{\parallel} is the parallel component. The black solid line is the lowest $\sqrt{\langle(\Delta\xi_{\perp})^2\rangle} \propto t^{0.5}$ of $\varepsilon_0 = 10^{13.5}$ eV, 10^{14} eV, and $10^{14.5}$ eV. This result can be interpreted as Bohm diffusion in our simulation when we consider the transport of particles in a multiphase medium.

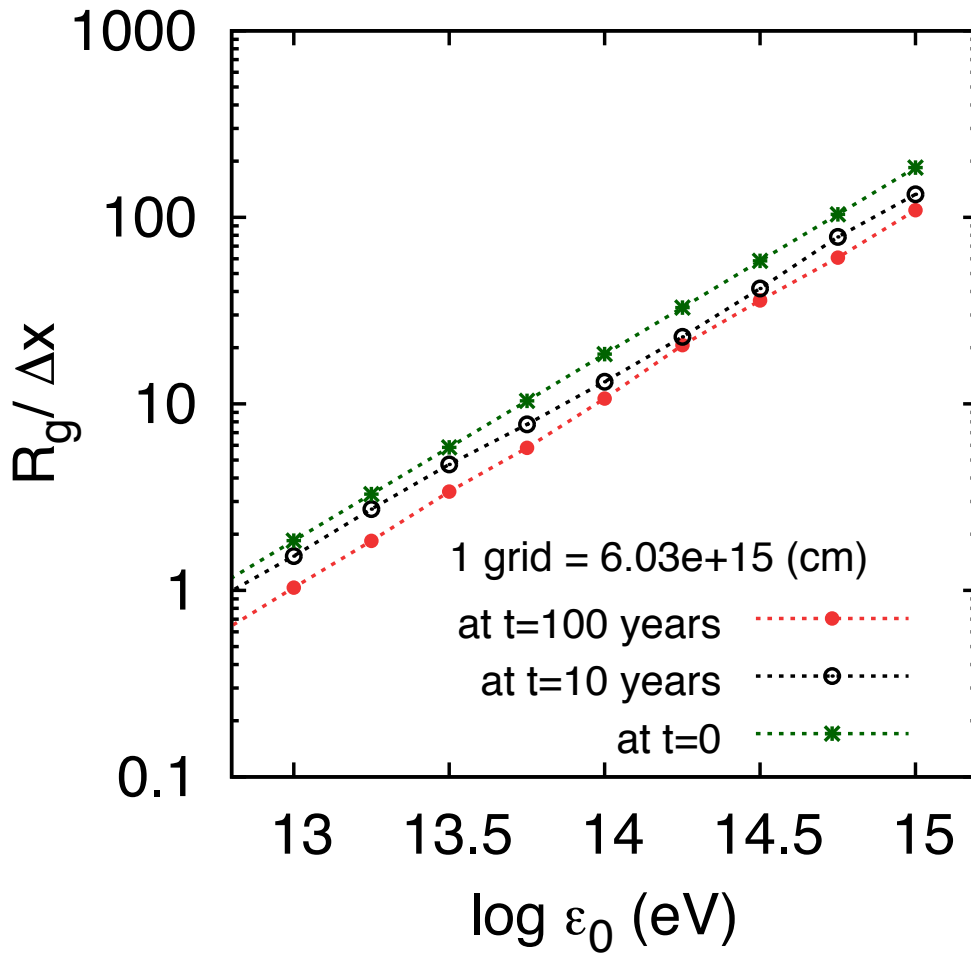


Figure 4.23: Gyroradius in units of pc, shown by dashed lines. The results at 10 years and 100 years are shown by open and filled black circles, respectively. Stars show the case $t=0$.

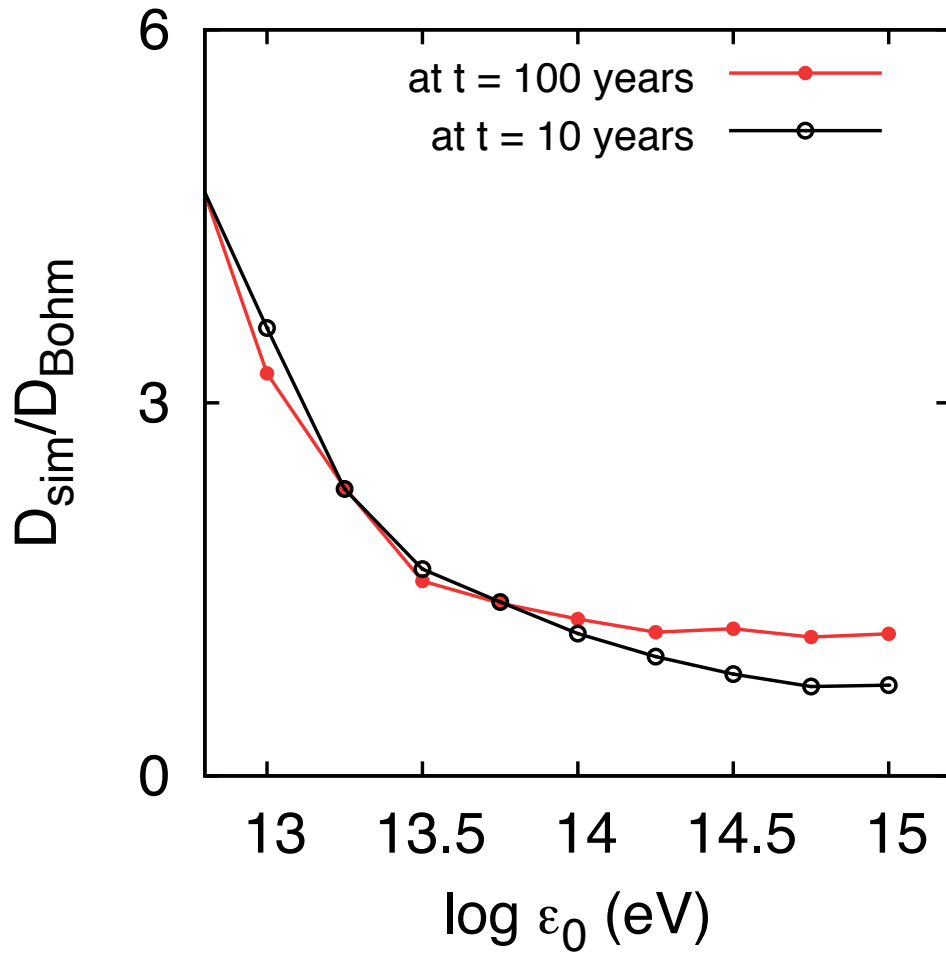


Figure 4.24: Ratio between simulation values (D_{sim}) and estimated values (D_{Bohm}) from Equations. 4.26 and 4.27, shown as a function of $\log \varepsilon_0$ by solid lines.

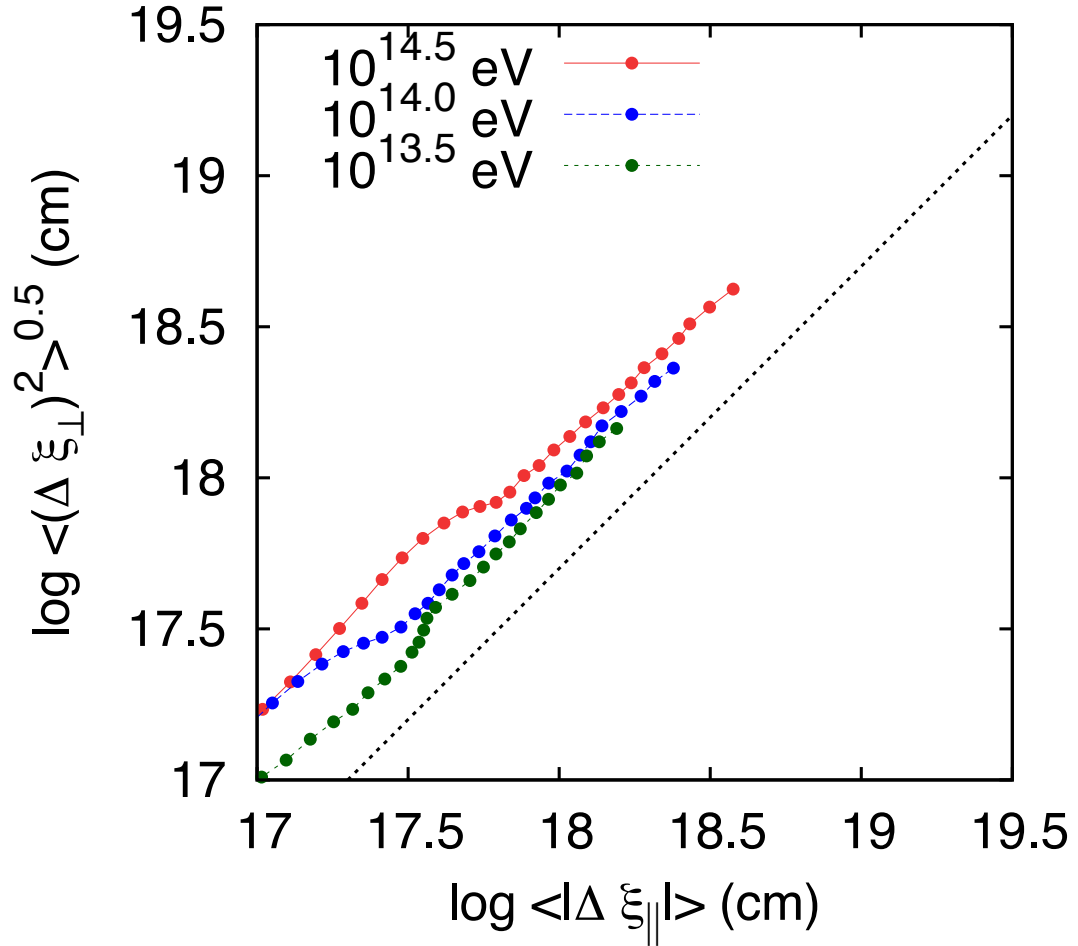


Figure 4.25: Relation between travel distances in the directions parallel and perpendicular to the mean magnetic field lines. $\langle (\Delta \xi_{\perp})^2 \rangle^{1/2}$ is shown as a function of $\langle |\Delta \xi_{\parallel}| \rangle$. The black dotted line indicates the slope $\propto \langle |\Delta \xi_{\parallel}| \rangle$. This figure shows no evidence of superdiffusion in multiphase media.

4.5 Magnetic Field Lines

A. Lazarian & H. Yan (2014) and S. Xu & H. Yan (2013) reported that diffusion is essentially determined by turbulent magnetic fields. They mentioned that superdiffusion takes place on scales smaller than the injection scale and motion is in the direction perpendicular to the magnetic field. To discuss this, an understanding of the structure of turbulent magnetic field lines is needed. The generation of turbulent magnetic fields strongly depends on diffusion processes. This section shows the magnetic field structures for two different media (T. Inoue et al. 2012; T. Inoue et al. 2013). I also discuss the reason for superdiffusion being observed in the one-phase medium by taking into account Richardson diffusion.

Figures. 4.26 and 4.27 show the magnetic field lines in our simulation box. The calculation is performed as follows:

$$\hat{\mathbf{B}}_x = \mathbf{B}_x / B, \quad (4.26)$$

$$d\mathbf{R} = \hat{\mathbf{B}}_x \Delta S, \quad (4.27)$$

$$\mathbf{R}^{n+1} = \mathbf{R}^n + d\mathbf{R}, \quad (4.28)$$

where ΔS indicates the constant distance along the magnetic field line. We fixed this distance to be 10^{14} cm for the calculation of magnetic field lines.

In Figures. 4.26 and 4.27, start points are marked with black dots on the magnetic field map. In the figures, magnetic field lines are represented by only 8 lines for each region. The multiphase medium case shows more complicated structures than the one-phase medium case. This is due to the difference in injection scales of turbulence in the two media.

The injection scale of the multiphase medium is about 0.2 pc, larger than the size of dense, cold clumps (~ 0.1 pc; see left of Figure. 4.28). As shown in Figure. 4.26, the field structure shows very complicated lines. This region can be explained by Figure. 4.27. The right panel of Figure. 4.28 shows the density (contour values are shown in the right axis of the figure in number density units). The yellow solid line represents one magnetic field line; it is bent by dense, cold clumps. This shows that the driving scale of magnetic field fluctuations is of the same scale as cold clouds. This might be the main difference between the magnetic field properties of one-phase and multiphase media. Therefore, we expect that Bohm diffusion can be observed in a multiphase medium.

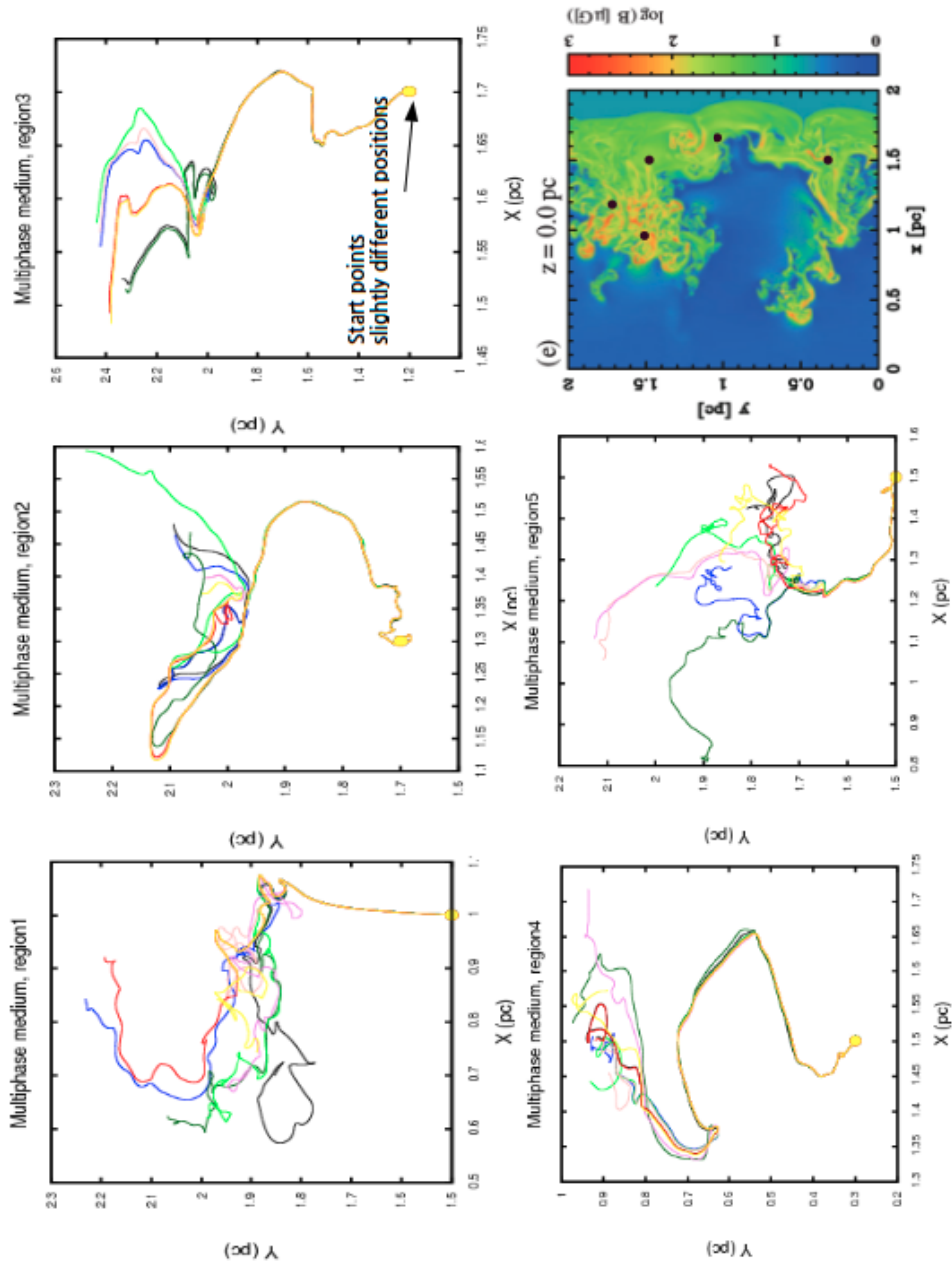


Figure 4.26: Magnetic Field lines (xy-plane) from T. Inoue et al. (2012) (multiphase medium). The black arrows indicate the start points. The start points are distributed within 1 grid size. 8 lines are used for each figure. The black dots of the bottom right panel indicate the start regions.

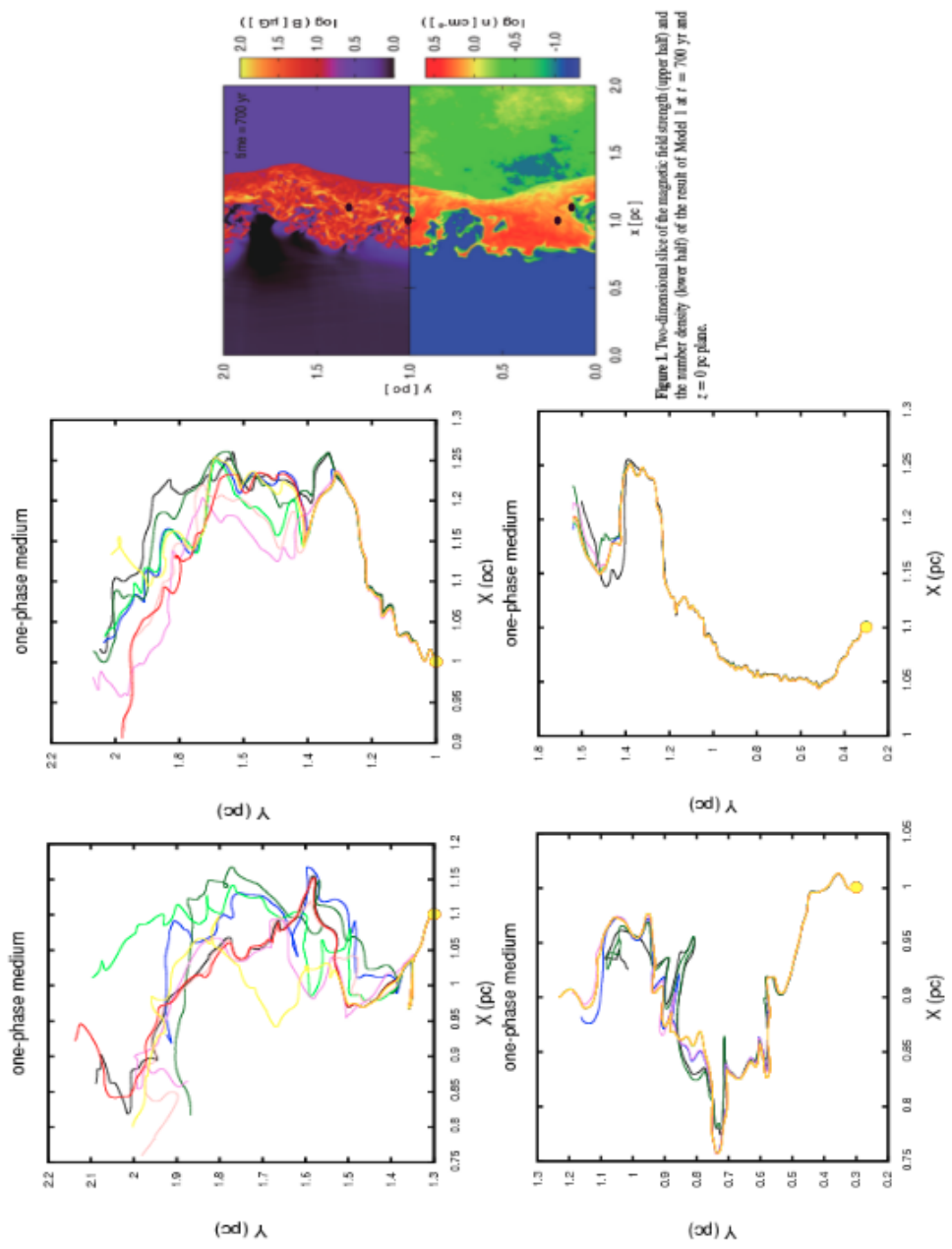


Figure 4.27: Magnetic Field lines (xy-plane) from T. Inoue et al. (2013) (one-phase medium).

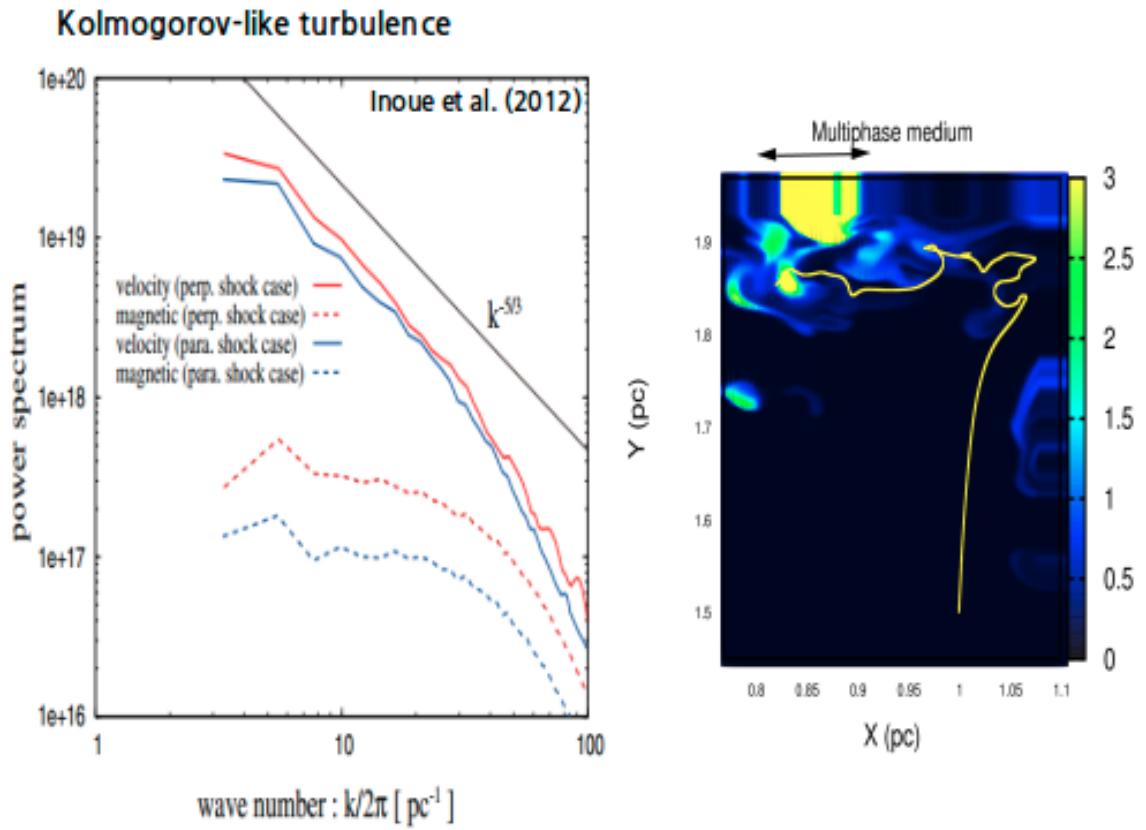


Figure 4.28: Kolmogorov spectrum and field line in multiphase medium. The black arrow of right figure indicates the size of clump (yellow color thin line).

It can be interpreted that the diffusion process strongly relies on the magnetic field strength because the gyrodaii of CRs are smaller than in previous cases due to the strong magnetic field. Therefore, particle travels along the magnetic field lines as in standard diffusion, $\propto t^{0.5}$.

Chapter 5

Summary and Future Work

Summary

Supernova remnants (SNRs) have long been believed to be the source of hadronic Galactic cosmic rays (GCRs) up to energies of the ‘knee’, near 5×10^{15} eV, of the cosmic ray (CR) spectrum. Supernova explosions forming collisionless shock waves induce the shocked gas and relativistic particles (hereafter cosmic rays) that produce multi-wavelength thermal and nonthermal emission. Diffusive shock acceleration (DSA) is the most promising mechanism for converting the kinetic energy of a supernova explosion into energetic particles and plays an important role in nonthermal emission during the overall process. DSA in SNR shocks is associated with transport processes, and some of the highest-energy CRs eventually escape from their acceleration sites by a diffusion process due to interactions with turbulent magnetic fields. If fast diffusion takes place in the accelerator, it indicates inefficient acceleration. Therefore, it is impossible to explain the observed rapid acceleration using standard theory.

A recent report on observations from the Fermi satellite has shown a signature of pion decay in the gamma ray spectra of SNRs. This provides strong evidence for protons accelerated in middle-aged SNRs interacting with molecular clouds. The origin of gamma rays can be interpreted as the decay of neutral pions produced by CR protons that encounter the dense region of accelerators such as molecular clouds. CR electrons emit synchrotron radiation in the X-ray range, but the X-ray and gamma ray distributions significantly differ. Therefore diffusion coefficients for the various CR particles are required in order to understand these differences. Also, according to recent observation of X-ray, it represented possibility of fast acceleration via a year time duration of synchrotron emission.

The interstellar medium (ISM) is an inhomogeneous, multiphase system in which gases of different temperatures, densities, and ionization fractions can coexist in approximate pressure equilibrium. It is a multiphase medium and remain clumpy by thermal instability driven by the compression process and radiative heating and cooling. We investigated the diffusion of CRs using a hydrodynamics simulation of a strong shock wave propagating in a realistic multiphase ISM. A blast wave generated by supernova expansion sweeps up the dense and clumpy HI clouds of the multiphase ISM and eventually generates strong velocity shear in the magnetic fields. Magnetic fields undergo amplification from their typical strength of μG to mG due to the turbulent dynamo in the post-shock region.

In order to quantitatively analyze the diffusion of high-energy CRs, we performed test particle numerical simulations that describe the propagation process of high-energy CR particles in the post-shock region where a blast wave interacts with both one-phase medium considering only simple density fluctuations and a realistic ISM.

Second order Fermi acceleration in energy space is expected in a turbulent medium. In our simulation, CRs energy gain is less than 1% of the original energy. Therefore, second-order Fermi acceleration is not available to occur in realistic environment due to small CRs diffusion coefficient although we observed in our simulation. In one-phase medium for our test-calculation, we found the existence of superdiffusion, which is faster than randomwalk in our simulation, whereas the differences of diffusion coefficient in simulation and estimated by Bohm show small. This superdiffusion appearance depends on the injection scale of turbulent energy.

On the other hand, a realistic ISM study represents that CRs diffusion process can be explained by slowest diffusion (so-called Bohm diffusion) due to large fluctuation of it. Efficient acceleration of CRs requires a small diffusion coefficient. Therefore, a result that may support the interpretation of high-energy emission from SNRs and assumption of T. Inoue et al. (2012).

Future Work

DSA depends on the diffusion coefficient in configuration space for CRs based on the assumption of isotropic scattering. The diffusion of plasma across a magnetic field was conjectured to follow Bohm diffusion, modelled as a random walk. Bohm diffusion, employed to replace the diffusion coefficient in the transport equation is proportional to λv , where λ and v are the mean scattering length and the particle velocity, respectively. To investigate this Bohm diffusion in our simulation, we will put the small scale turbulent using superposed Alfvén waves. Because, our simulation system is limited by grid size. We predict that the Bohm diffusion in a grid system. Also, we will investigate new acceleration mechanism from our simulation

data based on realistic environment. One of possible acceleration is shear field acceleration. For the test calculation, we found some crucial criterion. Therefore, we expect to get similar result by applied that criterion to our simulation data.

-Calculation of diffusion coefficient and synchrotron emission for CR electrons: We have already considered the diffusion coefficient for CR protons. This should also be done for CR electrons to investigate the difference in the diffusion processes of protons and electrons. Our result may quantitatively describe how synchrotron emission from CR electrons should be more localized to acceleration sites than gamma ray emission.

-Improvement of resolution of numerical simulations by considering small-scale structure in a grid: The system resolution of our 3-D simulation is determined by uniform grid cells, and the smallest turbulent scale is limited to a few grids. If particles exist within a smaller scale, they only encounter an almost uniform field and thus are expected to experience EXB drift. In this case the standard model of random walk is not supported because the travel distance is simply proportional to time at early times. To discuss the diffusion process at smaller scales with a more accurate model, we will perform test particle simulations accounting for arbitrary superposed Alfvén waves with small-scale turbulence.

-Consideration of numerous particles with use of an ensemble particle: Heretofore, we have calculated the trajectories and physical properties of single particle transport in a multiphase medium because we assumed a collisionless environment due to a

low-density background. In reality one has to account for millions of particles, but in that case an enormous amount of calculation time is consumed. To alleviate this problem, we devise an ensemble particle which is assigned to a single particle to represent numerous particles. Eventually, the trajectory and energy distribution of numerous particles can be recovered by counting ensemble particles and using statistical methods. We expect that a new model can be established through comparing nonthermal radiation data and the results from the ensemble particle method.

-Confirm whether or not the exclusion of cosmic rays due to stellar wind is true: For the development of magnetorotational instability (MRI) driven mass accretion in a protoplanetary disk, a sufficient ionization degree is needed. CRs are believed to be an ionization source for protoplanetary disk gas. In the solar system, propagation of CRs is inhibited by magnetized winds, i.e., the heliosphere. The solar wind strongly modulates CRs within the heliosphere. Based on this, L. I. Cleeves et al.(2013) investigated how CR exclusion affects the ionization rate in protoplanetary disks. An ionization rate was computed from CR fluxes estimated by CR modulation using spot coverage of the Sun. For a T-Tauri star, the ionization rate is obtained by extrapolating CR modulation due to solar activity assuming 2-8 % spot coverage. The resultant integrated CR ionization rate is 3 orders of magnitude smaller than the interstellar value that is used for protoplanetary disks. However, the problem is that this result cannot explain the observed mass accretion rate. Thus, I propose to estimate the ionization degree more precisely by calculating CR propagation in solar wind. Also, I would like to investigate whether or not CR exclusion due to solar wind

is true. This can be done using solar wind simulation data from T. Suzuki & S. Inutsuka (2006) and our already-developed simulation code to calculate the trajectories and physical properties of particles. From the results of our ionization degree calculations, we can discuss the chemical composition of protoplanetary disk gas.

Appendix A

Dynamics of charged particle motion in Electromagnetic Fields

Motion of Charge Particles

The motion of charged particles in the presence of electromagnetic field is well known as functions of position and time. We consider the fields to be constant in time and spatially uniform. We considered that the electric and magnetic fields are not affected by the charged particles. The study of the motion of charged particles in specified fields is important, since it provides a good physical understanding of the dynamical processes in plasma. The equation of motion for a particle of charge q , under the action of the Lorentz force \mathbf{F} due to electric field \mathbf{E} and magnetic field \mathbf{B} are written as

$$\frac{d\mathbf{p}}{dt} = \mathbf{F} = q(\mathbf{E} + \mathbf{v} \times \mathbf{B})/c \quad (5.1)$$

where, \mathbf{p} is the momentum of the particle and \mathbf{v} is velocity of particle. This equation is relativistic correct it, then we take

$$\mathbf{p} = \gamma m \mathbf{v} \quad (5.2)$$

where m is the rest mass of the particle and γ is the Lorentz factor defined by

$$\gamma = \left(1 - \frac{v^2}{c^2}\right)^{-1/2} \quad (5.3)$$

where c is the speed of light in the vacuum. Then, in the relativistic case, it can be written in the form

$$\gamma m \frac{d\mathbf{v}}{dt} + q \frac{\mathbf{v}}{c^2} (\mathbf{v} \cdot \mathbf{E}) = q(\mathbf{E} + \mathbf{v} \times \mathbf{B})/c \quad (5.4)$$

Here, it can be neglected the term of $\frac{v^2}{c^2}$ by comparing with unity. For $\frac{v^2}{c^2} \ll 1$ we have $\gamma \simeq 1$ and mass of particle (m) can be considered constant, so that we can reduce to the following non-relativistic expression,

$$m \frac{d\mathbf{v}}{dt} = \mathbf{F} = q(\mathbf{E} + \mathbf{v} \times \mathbf{B})/c \quad (5.5)$$

Energy conservation

In the absence of an electric field ($\mathbf{E} = 0$), the equation of motion can be reduced to

$$m \frac{d\mathbf{v}}{dt} = \mathbf{F} = q \left(\frac{\mathbf{v} \times \mathbf{B}}{c} \right) \quad (5.6)$$

Since the magnetic force is perpendicular to \mathbf{v} , it does not work on the particle. Taking the dot product of this equation with v and noting that for any vector \mathbf{v} , we have $(\mathbf{v} \times \mathbf{B}) \cdot \mathbf{v} = 0$, since $(\mathbf{v} \times \mathbf{B})$ is perpendicular to \mathbf{v} . We obtain,

$$m \frac{d\mathbf{v}}{dt} \cdot \mathbf{v} = \frac{d}{dt} \frac{1}{2} m v^2 = 0 \quad (5.7)$$

which shows that the particle kinetic energy ($mv^2/2$) and the magnitude of its velocity (v) are both constants. Therefore, a static

magnetic field does not change the particle kinetic energy. However, if \mathbf{B} varies with time, then according to Maxwell equations, an electric field such that $\nabla \times \mathbf{E} = -\frac{\partial \mathbf{B}}{\partial t}$ is also present which does work on the particle changing its kinetic energy. Total relativistic energy is $U = \gamma mc^2$ given by

$$\frac{dU}{dt} = q(\mathbf{v} \cdot \mathbf{E}) \quad (5.8)$$

and,

$$\frac{dP}{dt} = \frac{Uv}{tc^2} \quad (5.9)$$

When both \mathbf{E} and \mathbf{B} are present, we obtain

$$m \frac{d\mathbf{v}}{dt} = q\left(\mathbf{E} + \frac{\mathbf{v} \times \mathbf{B}}{c}\right) \quad (5.10)$$

$$\frac{d}{dt}\left(\frac{1}{2}mv^2\right) = q(\mathbf{B} \cdot \mathbf{v}) \quad (5.11)$$

Since, $\nabla \times \mathbf{E} = 0$, then $\mathbf{E} = -\nabla\phi$.

$$\frac{d}{dt}\left(\frac{1}{2}mv^2\right) = -q(\nabla\phi) \cdot \mathbf{v} \quad (5.12)$$

$$-q(\nabla\phi) \cdot \frac{d\mathbf{r}}{dt} = -q\left(\frac{d\phi}{dt}\right) \quad (5.13)$$

Therefore,

$$\frac{d}{dt}\left(\frac{1}{2}mv^2 + q\phi\right) = 0 \quad (5.14)$$

At static field, kinetic energy of particles and energy of electric field are constant.

Drift motion

We assumed the motion of the charged particle is perpendicular to the direction of \mathbf{B} (z-direction). Also, the direction of \mathbf{B} is perpendicular to direction of \mathbf{E} (x-direction).

$$\mathbf{F} = q(\mathbf{E} + \mathbf{v} \times \mathbf{B})/c \quad (5.15)$$

Particles drawn to move along y-direction due to $\mathbf{E} \times \mathbf{B}$ drift motion: motion of particle is perpendicular to \mathbf{E} and \mathbf{B} .

1. At first, magnetic force is zero ($v = 0$), so electric field force accelerates toward z-direction.
2. Then, magnetic force is occurred due to velocity generated by acceleration of z-direction, $qv_z B_x = F_y$.
i.e). More velocity of particle is fast, the more F_y got bigger.
3. Hence, motion of particle is apt to return. \mathbf{B} provides the centripetal force required for circular motion. If magnetic force increases, time period get shorter.
4. Using Equation. 5.15 we can get,

$$R = \frac{E}{\omega B} \quad (5.16)$$

$$v = \omega R = \frac{E}{B} \quad (5.17)$$

$$\mathbf{v} = c \frac{\mathbf{E} \times \mathbf{B}}{B^2} \quad (5.18)$$

Particles move to y-direction with radius R Equation. 5.16 and constant velocity v Equation. 5.17. *c.f*). Equation. 5.18 is actual drift velocity. This velocity is independent of charge and mass.

Acknowledgement

The author would like to thank Professor Dr. Shu-ichiro Inutsuka for his continuous support and encouragement. The thesis could not have been accomplished without his support. The author would like to thank Professor Jennifer Ston for her careful reading of this manuscript and numerous constructive remarks. She is also grateful to Dr. Tsuyoshi Inoue, Takeru K. Suzuki, Kazunari Iwasaki and Takuma Matsumoto for their kind assistance and for valuable discussions about this research project. Moreover, she wishes to thank Hiroshi Kobayashi, Yusuke Tsukamoto, Hiroyuki Kurokawa for variable supports and advises over the doctoral course. She would like to express deep gratitude to past and present members of theoretical astrophysics group. I need to mention her name Fujii Yuri, I was always together during whole of doctoral course. Finally, the author wishes to thank to her parents for their unconditional supports both before and during the doctoral course.

Bibliography

- Abdo, A.A. et al. (Fermi LAT Collaboration), (2009) *ApJ*, 706, L1
- Abdo, A.A. et al. (Fermi LAT Collaboration), (2010a) *ApJ*, 712, 459
- Abdo, A.A. et al. (Fermi LAT Collaboration), (2010b) *ApJ*, 718, 348
- Abdo, A.A. et al. (Fermi LAT Collaboration), (2010c) *Science*, 327, 1103
- Ackermann, M., Ajello, M., Allafort, A., et al., (2013) *Science*, 339, 807
- Aharonian, F.A., & Atoyan, A.M., (1996) *AAP*, 309, 917
- Aharonian, F. et al., (2006) *Nature*, 439, 695
- Axford, W.I., et al., (1977) *Proceedings 15th International Cosmic Ray Conference, Plovdiv*, 11, 132.
- Axford W.I., Leer E., McKenzie J.F., (1982) *A&A* 111, 317
- Ballantyne, D., Melia, F., & Liu, S., (2007) *ApJ Letters*, 657, L13
- Beck, R., *Space Sci. Rev.*, (2000) 99, 243
- Bell, A.R. (1978a), *MNRAS*, 182, 147, (1978b) *MNRAS*, 182, 443.

- Biermann, P.L., Strittmatter, P.A., (1987) *Astrophys. J.* 322, 643–649.
- Blandford, R., Eichler, D. (1987) *physrep*, 154, 1
- Blandford, R.D. & Ostriker, J.P., (1978) *ApJ.Lett.*, 221 L29.
- Casse, F., Lemoine, M., & Pelletier, G. (2002) *prd*, 65, 023002
- Cleeves, L.I. et al., (2013) *ApJ.* 772, 5
- Dosch, A., Shalchi, A., Tautz, R.C., (2011) *MNRAS*, 413, 2950
- Drury L.O'C, Volk H.J., (1981) *ApJ* 248, 344
- Duffy, P., (1992) *aap*, 262, 281
- Fatuzzo, M., Melia, F., Todd, E., & Adams, F.C., (2010) *ApJ*, 725, 515
- Fazio, G.G., (1967) *ARA*, 5, 481
- Field, G.B., (1965) *ApJ*, 142, 531
- Fukui, Y., (2013) *Cosmic Rays in Star-Forming Environments*, 34, 249
- Giacinti, G., & Sigl, G., (2012) *Physical Review Letters*, 109, 071101
- Giacalone, J., & Jokipii, J.R., (1999) *ApJ*, 520, 204
- Hanabata, Y., Katagiri, H., Hewitt, J.W., et al., (2014) *ApJ*, 786, 145
- Hayakawa, S., (1952) *Prog. Theor. Phys*, 8, 571
- Hillas, A.M., (1984) *Ann. Rev. Astro. Astrophys.* 22, 425-444.

- Hoshino, M., (2012) *Physical Review Letters*, 108, 135003
- Hussein, M., & Shalchi, A., (2014) *ApJ*. 785, 31
- Inoue, T., Yamazaki, R., & Inutsuka, S., (2010) *ApJl*, 723, L108
- Inoue, T., Yamazaki, R., Inutsuka, S., & Fukui, Y., (2012) *ApJ*. 744, 71
- Inoue, T., Shimoda, J., Ohira, Y., & Yamazaki, R., (2013) *ApJl*, 772, LL20
- Kang, H., & Jones, T.W., (2004) *Journal of Korean Astronomical Society*, 37, 405
- Kang, H., Ryu, D., Jones, T.W., (1996) *ApJ*. 456, 422–427.
- Kirk, JR and Dendy, RO., (2001) *Nucl. Part. Phys.* 27, 1589-1595
- Kotera, K., Olinto, A.,(2011) *Ann. Rev. Astron. Astrophys.* 49, 119–153.
- Koyama K., Petre R., Gotthelf E.V, Hwang, U., Matsuura M., Ozaki M., Holt S.S., 1995, *Nature* 378 255
- Knapp, J. et al., (2003) *Astropart. Phys.* 19, 77–99.
- Lazarian, A., & Yan, H. (2014) *ApJ*, 784, 38
- Myers, P.C., (1978) *ApJ*, 225, 380
- Muranushi, T., & Inutsuka, S.i., (2009) *ApJl*, 691, L24
- Ohira, Y., Murase, K., & Yamazaki, R., (2011) *MNRAS*, 410, 1577

- Ohira, Y., Yamazaki, R., Kawanaka, N., & Ioka, K. (2012) MNRAS, 427, 91
- Rossi, B., Greisen, K. (1941) Rev. Mod. Phys. 13, 240–309.
- Shalchi, A., (2009) APh 31, 237-242.
- Shalchi, A., *Nonlinear Cosmic Ray Diffusion Theories*
- Skilling, F., (1975) MNRAS, 172, 557
- Stage, M.D., Allen, G.E., Houck, J.C., & Davis, J.E., (2006) Nature Physics, 2, 614
- Stecker, F. W., (1969) Nature, 222, 5196
- Tavani, M. et al., (2010) ApJ, 710, L151
- Uchiyama, Y., Aharonian, F.A., Tanaka, T., Takahashi, T., & Maeda, Y., (2007) Nature, 449, 576
- V. Berezhinsky, A. Gazizov, S.I. Grigor'eva, (2006) Phys. Rev. D. 74, 043005.
- Waxman, E., (1995) Phys. Rev. Lett. 75, 386–389.
- Wommer, E., Melia, F., & Fatuzzo, M., (2008) MNRAS, 387, 987
- Xu, S., & Yan, H., (2013) ApJ. 779, 140
- Zank, G.P., Li, G., Florinski, V., et al., (2006) Journal of Geophysical Research (Space Physics), 111, A06108